

# Liquidus Phase Relations in the CaO–MgO–Al<sub>2</sub>O<sub>3</sub>–SiO<sub>2</sub> System at 3·0 GPa: the Aluminous Pyroxene Thermal Divide and High-pressure Fractionation of Picritic and Komatiitic Magmas

CHENEY S. MILHOLLAND\* AND DEAN C. PRESNALL†

MAGMALOGY LABORATORY, DEPARTMENT OF GEOSCIENCES,  
THE UNIVERSITY OF TEXAS AT DALLAS, P.O. BOX 830688, RICHARDSON, TX 75083-0688, USA

RECEIVED FEBRUARY 10, 1997; REVISED TYPESCRIPT ACCEPTED JULY 23, 1997

*We present liquidus phase equilibrium data at 3·0 GPa for the model tholeiitic basalt tetrahedron, diopside–anorthite–forsterite–quartz, in the CaO–MgO–Al<sub>2</sub>O<sub>3</sub>–SiO<sub>2</sub> system. This pressure coincides with the invariant point (1568°C) on the simplified model lherzolite solidus that marks the transition between spinel lherzolite and garnet lherzolite (fo + en + di + sp + gt + liq). The composition of the liquid at the invariant point (46·4 An, 16·0 Di, 33·5 Fo, 4·2 Qz, wt %) is a model olivine-rich basalt that lies slightly (0·2% excess fo) to the SiO<sub>2</sub>-poor side of the aluminous pyroxene plane, MgSiO<sub>3</sub>–CaSiO<sub>3</sub>–Al<sub>2</sub>O<sub>3</sub>. A large garnet primary phase volume is bordered by primary phase volumes for forsterite, spinel, sapphirine, corundum, enstatite, diopside, quartz, and kyanite. The observed absence of enstatite at the solidus of lherzolite at pressures above ~3·3 GPa is readily understood from the phase relations in this system. During melting at these high pressures, enstatite first forms at a temperature somewhat above the solidus and then dissolves before complete melting. As pressure increases above 3·0 GPa, the aluminous pyroxene plane, MgSiO<sub>3</sub>–CaSiO<sub>3</sub>–Al<sub>2</sub>O<sub>3</sub>, becomes increasingly effective as a thermal divide that causes picritic and komatiitic melts lying on the silica-poor side of the plane to fractionate toward alkalic picritic compositions. However, if the rate of ascent of these melts is sufficiently rapid, expansion of the olivine primary phase volume as pressure decreases produces a fractionation trend dominated by olivine crystallization and the thermal divide is ignored.*

KEY WORDS: high pressure; fractionation; komatiite; basalt; thermal divide

## INTRODUCTION

In the CaO–MgO–Al<sub>2</sub>O<sub>3</sub>–SiO<sub>2</sub> (CMAS) system, the tetrahedron diopside–anorthite–forsterite–quartz (Di–An–Fo–Qz) is a simplified analog of the tholeiitic portion of the basalt tetrahedron of Yoder & Tilley (1962) and has been used extensively to model the melting behavior of the Earth's mantle and the fractional crystallization of basalts. Here, we present a study of liquidus phase relations in this system at 3·0 GPa. By chance, we have found that the univariant transition curve for the spinel lherzolite (olivine + enstatite + diopside + spinel) to garnet lherzolite (olivine + enstatite + diopside + garnet) assemblage, as it intersects the solidus, occurs exactly at 3·0 GPa. Thus, we are able to clarify in some detail the changes in melting and crystallization behavior that occur as this transition is crossed. We discuss the bearing of these phase relations on the aluminous pyroxene thermal divide and high-pressure fractional crystallization of komatiitic and picritic magmas.

## EXPERIMENTAL PROCEDURE

Piston-cylinder presses at the University of Texas at Dallas were used for all experiments. The sample assembly is the same as that described by Presnall *et al.* (1978), except that a Pyrex glass sleeve was used instead of boron nitride

\*Present address: 1 Summer Haven, Madisonville, LA 70447, USA

†Corresponding author.

and a crushable alumina spacer rod was used in some of the runs instead of fired pyrophyllite. Temperatures were measured with W3Re/W25Re or W5Re/W26Re thermocouples, and were not corrected for the effect of pressure on e.m.f. Temperatures are referenced to the International Temperature Scale of 1990 (ITS-90, Preston-Thomas, 1990) and were controlled automatically within  $\pm 3^\circ\text{C}$ . The hot piston-out procedure (Presnall *et al.*, 1978) was used with no pressure correction applied. Pressure and temperature uncertainties are  $\pm 0.05$  GPa and  $\pm 10^\circ\text{C}$ , which have been found by experience to be appropriate to obtain internally consistent data (Presnall *et al.*, 1979). We have used glass or partly crystalline starting mixtures (Table 1) from previous studies (Chen & Presnall, 1975; Presnall, 1976; Presnall *et al.*, 1978, 1979; Liu & Presnall, 1990), and several mixtures prepared by J. D. Dixon (DAFQ labels) and by us using the methods of Presnall *et al.* (1972). After each run, the platinum capsule containing the charge was mounted in epoxy and ground down to about one-half the depth of the capsule to expose a longitudinal section of the cylindrical run product. The exposed surface was polished for microscopic examination and microprobe analysis. Phases were identified by a combination of reflected light microscopy, backscattered electron imaging, and wavelength-dispersive chemical analysis. All microprobe work was done on a JEOL JXA-8600 Superprobe at the University of Texas at Dallas. Analytical conditions were an accelerating voltage of 15 kV and a beam current of 20 nA. The electron beam was focused ( $\sim 2$   $\mu\text{m}$  diameter) for minerals and small pockets of glass, and defocused at 15  $\mu\text{m}$  when analyzing larger areas of glass.

## ATTAINMENT OF EQUILIBRIUM

To determine if our experiments are long enough to attain equilibrium, we rely on reversal experiments that are independent of the glassy or crystalline state of the starting mixture. First, two runs are made that closely bracket a liquidus temperature. Then a second pair of runs is made to demonstrate reversibility. One sample is held below the liquidus temperature for a time long enough to obtain a crystal + liquid assemblage, as demonstrated in the initial bracketing runs; and then, without taking the sample out of the apparatus, the temperature is raised above the liquidus and held for the same amount of time. This procedure is then repeated in the down-temperature direction. Because these reversal experiments are very time-consuming, it has been the practice in this laboratory to reverse only a representative liquidus bracket for each primary phase field. A number of these reversals have been done in this laboratory at lower pressures where temperatures are lower and reaction rates are generally slower. On the basis of these

earlier studies, times required for equilibrium have been established as 2 h for spinel at  $1520^\circ\text{C}$ , 4 h for forsterite at  $1494^\circ\text{C}$ , 2 h for diopside at  $1401^\circ\text{C}$  (Presnall *et al.*, 1978), 5 h for enstatite at  $1540^\circ\text{C}$ , 24 h for quartz at  $1490^\circ\text{C}$ , and 6 h for sapphirine at  $1410^\circ\text{C}$  (Liu & Presnall, 1990). In the present study, a time of 6 h has been established for garnet at  $1580^\circ\text{C}$  (Table 2). We assume that runs for these durations at similar or higher temperatures and on similar bulk compositions yield equilibrium phase assemblages. For the corundum primary phase field, Presnall *et al.* (1978) failed to achieve reversals of experiments lasting 50 h. Also, we have failed to reverse the kyanite primary phase field in experiments lasting 24 h. Therefore, runs containing these phases should be considered synthesis experiments. Also, the durations for runs 526-1, 524-3, and 518-4 (Table 3) are shorter than the reversed durations, but the results of these runs appear to be consistent with those of other equilibrium runs.

## PHASE RELATIONS

In presenting the configuration of liquidus primary phase volumes in the system Di-An-Fo-Qz at 3 GPa (Fig. 1), we first describe new data on (1) the An-Fo-Qz base, (2) the Di-An-Fo face, (3) the Di-An-En join within the tetrahedron, and (4) the aluminous pyroxene plane,  $\text{MgSiO}_3$ - $\text{CaSiO}_3$ - $\text{Al}_2\text{O}_3$ , part of which cuts through the tetrahedron. With the aid of these ternary joins and 15 additional compositions that do not lie on a specific join, we then describe quaternary phase relations in the tetrahedron.

### Anorthite-forsterite-quartz

Phase relations on the An-Fo-Qz join have previously been studied at 1 atm (Andersen, 1915; Irvine, 1975; Longhi, 1987), 1.0 GPa (Sen & Presnall, 1984), 2.0 GPa (Liu & Presnall, 1990) and 2.8 GPa (Adam, 1988). These studies indicate that with increasing pressure, the forsterite (fo) and anorthite (an) primary phase fields shrink and the corundum (co), enstatite (en), and quartz (qz) primary phase fields expand. A major change in the phase relations between 1.0 and 2.0 GPa is the presence of a sapphirine (sa) field at 2.0 GPa (Liu & Presnall, 1990). Also, O'Hara (1965, 1968), Kushiro (1968), Chen & Presnall (1975), Presnall *et al.* (1978, 1979), Stolper (1980), and Sen & Presnall (1984) have discussed the shift of the boundary line between fo and en away from the qz apex as pressure increases. A large garnet (gt) primary phase field within the an-fo-qz join at 3.0 GPa is indicated by the results of Davis & Schairer (1965) at 4.0 GPa and Adam (1988) at 2.8 GPa.

Table 1: Compositions of starting mixtures (wt %)

Mixture	Di	An	Fo	En	Py <sub>2</sub> Gr	Qz
GS-0		55.00	35.00			10.00
GS-1		45.00	42.00			13.00
GS-3		52.00	15.00			33.00
GS-6		60.00	12.00			28.00
GS-11		64.00	23.00			13.00
AFQ-20		55.00	20.00			25.00
AFQ-22		50.00	42.00			8.00
AFQ-23		65.00	8.00			27.00
AFQ-24		68.00	13.00			19.00
AFQ-25		72.00	19.00			9.00
AFQ-26		70.00	4.00			26.00
AFQ-28		72.00	14.00			14.00
AFQ-30		50.00	45.00			5.00
AFQ-31		45.00	47.00			8.00
AFQ-32		68.00	25.00			7.00
AFQ-33		64.00	14.00			22.00
AFQ-34		50.00	30.00			20.00
AFQ-35		48.00	45.00			7.00
AFQ-36		51.00	23.00			26.00
DFA-4	70.00		30.00			
DFA-18	10.00	80.00	10.00			
DFA-24	20.00	60.00	20.00			
DFA-31	10.00	60.00	30.00			
DFA-32	35.00	35.00	30.00			
DEA-1	15.00	55.00		30.00		
DEA-2	15.00	65.00		20.00		
DEA-3	20.00	70.00		10.00		
DEA-25	10.00	45.00		45.00		
DEA-29	15.00	46.00		39.00		
CMAS-7	21.00	48.00		31.00		
DEG-24	15.02			27.46	57.52	
DEG-26	10.00			20.00	70.00	
DEG-27	15.00			25.00	60.00	
DEG-28	12.00			22.00	66.00	
DEG-32	14.00			19.00	67.00	
DEG-33	16.00			15.00	69.00	
DEG-34	18.00			17.00	65.00	
CMAS-4	16.56	52.44	22.83			8.17
CMAS-5	14.86	49.82	28.19			7.13
CMAS-6	8.16	37.00	46.46			8.38
CMAS-8	13.65	40.51	41.07			4.77
CMAS-10	12.00	55.80	17.90			14.30
CMAS-11	27.50	42.60	12.30			17.60
CMAS-12	6.00	58.00	12.00			24.00
CMAS-17	15.02	49.72	29.75			5.51
CMAS-18	9.99	58.51	24.75			6.75
CMAS-20	17.89	48.66	27.44			6.01
CMAS-21	7.00	63.39	16.60			13.01
CMAS-22	5.21	61.48	18.10			15.21
DAFQ-23	9.98	45.02	40.00			5.00
DAFQ-30	15.00	44.00	37.00			4.00
DAFQ-31	13.00	50.00	22.00			15.00

Abbreviations: Di, CaMgSi<sub>2</sub>O<sub>6</sub>; An, CaAl<sub>2</sub>Si<sub>2</sub>O<sub>8</sub>; Fo, Mg<sub>2</sub>SiO<sub>4</sub>; En, MgSiO<sub>3</sub>; Py<sub>2</sub>Gr, CaMg<sub>2</sub>Al<sub>2</sub>Si<sub>3</sub>O<sub>12</sub>; Qz, SiO<sub>2</sub>.

The phase diagram for the An–Fo–Qz join at 3.0 GPa (Fig. 2) is based on quenching experiments on 32 mixtures within this join (Table 3). Phase relations in the bounding

system, Fo–Qz, at 3.0 GPa are similar to those reported by Chen & Presnall (1975) at 2.5 GPa except that at 3.0 GPa, liquidus temperatures are higher and the forsterite–

Table 2: Reversal experiments

Run	Mixture	Initial condition		Final condition		Phases
		T (°C)	Duration (h)	T (°C)	Duration (h)	
523-3	GS-0	1580	6	1640	6	gl
529-2	GS-0	1640	6	1580	6	gl + gt

Phase abbreviations: gl, glass; gt, garnet.

enstatite eutectic composition is slightly more Fo rich (Presnall *et al.*, 1998). The melting temperature of anorthite composition,  $\sim 1900^\circ\text{C}$ , is based on a linear extrapolation from data of Lindsley (1968) at 1 and 2 GPa. The forsterite melting temperature, corrected to ITS-90, is  $2041^\circ\text{C}$  (Davis & England, 1964). Within the An–Fo–Qz join, we find primary phase fields for forsterite, enstatite, quartz, spinel, garnet, corundum, and kyanite, and intersections of these fields define the locations of seven piercing points (Table 4).

On the basis of electron microprobe analyses, the aluminum silicate phase found in our run products is stoichiometric  $\text{Al}_2\text{SiO}_5$ . Although we have not identified the  $\text{Al}_2\text{SiO}_5$  polymorph, extrapolation of the sillimanite–kyanite boundary from lower temperatures and pressures indicates that the stable aluminum silicate phase is kyanite (Holdaway, 1971).

Liquidus phase relations on the join An–Fo–Qz at 2.8 GPa reported by Adam (1988) indicate the presence of primary phase fields of forsterite, enstatite, spinel, garnet, and corundum, and the configuration of these fields is similar to ours (Fig. 3). The main difference is in the region where the primary phase fields of forsterite, enstatite, spinel, and garnet come together. Adam (1988) shows piercing points for the quaternary univariant boundary lines, fo + sp + gt + liq and fo + en + gt + liq, whereas we find piercing points for the quaternary univariant boundary lines, fo + en + sp + liq and en + sp + gt + liq. Adam's configuration indicates that the garnet primary phase field is expanded sufficiently to intersect the forsterite primary phase field, whereas our results indicate that the garnet field does not intersect the forsterite field. Because the garnet field expands with pressure, this difference suggests that the pressure of our study is slightly lower than that of Adam (1988), an apparent discrepancy. On the other hand, the spinel–forsterite boundary we find is closer to forsterite than that shown by Adam (1988). Because the spinel–forsterite boundary moves toward forsterite as pressure increases, the shift of this boundary suggests a slightly higher pressure for our study. Liquidus temperatures found by Adam (1988) are  $50\text{--}80^\circ\text{C}$  lower than ours, which also

suggests that our study is at a higher pressure than his. However, these temperature differences are somewhat larger than would be expected from a difference in pressure of only 0.2 GPa. Because (1) we have demonstrated with reversal experiments that our runs are long enough to achieve equilibrium, and (2) we have several starting compositions that tightly constrain the positions of boundary lines in the vicinity of the fo + en + sp + liq and en + sp + gt + liq piercing points, we believe our configuration of boundary lines at 3 GPa in this area is correct. The data of Adam (1988) are not as constraining and would allow the construction of phase boundaries that are consistent with ours.

An increase in pressure from 2 to 3 GPa causes significant changes in the liquidus phase relations within the An–Fo–Qz join (Fig. 4). The 2 GPa primary phase fields of anorthite and sapphirine disappear at 3 GPa, and a large primary phase field of garnet appears. However, in the tetrahedron diopside–anorthite–forsterite–quartz, it will be seen later that a sapphirine volume remains stable at 3 GPa. Because the garnet field expands with pressure and lies entirely on the silica-rich side of the aluminous pyroxene plane (represented on the An–Fo–Qz diagram by the  $\text{CaMg}_2\text{Al}_2\text{Si}_3\text{O}_{12}\text{--MgSiO}_3$  line in Figs 2 and 3) at 3 GPa, it must approach the aluminous pyroxene plane from the silica-rich side.

### Diopside–anorthite–forsterite

The liquidus surface of the Di–An–Fo join (Fig. 5) is based on data for one mixture on the Di–Fo join, four mixtures within the Di–An–Fo join (Table 3), and the An–Fo join from Fig. 2. Although our data are sparse, we find that the form of the liquidus surface is changed only slightly from that at 2.0 GPa given by Presnall *et al.* (1978). The temperature of the piercing point, fo + di + sp + liq, increases from  $1485^\circ\text{C}$  at 2.0 GPa (Presnall *et al.*, 1978) to  $\sim 1610^\circ\text{C}$  at 3.0 GPa. Also, the spinel and forsterite fields shrink relative to that of diopside, a continuation of the trend established at pressures below 2 GPa (Yoder & Tilley, 1962; Presnall

Table 3: Quenching experiments

Run	Mixture*	T (°C)	Time (h)	Phases
500-1	An <sub>95</sub> Fo <sub>5</sub>	1650	6	gl + co
500-2	An <sub>86</sub> Fo <sub>14</sub>	1700	6	gl + co
500-7	An <sub>80</sub> Fo <sub>20</sub>	1700	24	gl
500-6	An <sub>80</sub> Fo <sub>20</sub>	1685	6	gl + sp + (di)
500-9	An <sub>60</sub> Fo <sub>40</sub>	1740	6	gl
502-1	An <sub>60</sub> Fo <sub>40</sub>	1690	6	gl + sp + (di)
501-4	An <sub>54</sub> Fo <sub>46</sub>	1760	6	gl
501-3	An <sub>54</sub> Fo <sub>46</sub>	1740	6	gl + sp + (di)
506-1	An <sub>50</sub> Fo <sub>50</sub>	1740	6	gl + (di)
518-3	An <sub>50</sub> Fo <sub>50</sub>	1720	4	gl + sp + (di)
501-6	An <sub>45</sub> Fo <sub>55</sub>	1760	6	gl
502-4	An <sub>45</sub> Fo <sub>55</sub>	1740	6	gl + fo + (fo)
509-2	En <sub>87</sub> Qz <sub>13</sub>	1805	24	gl + qz
526-1	Fo <sub>20</sub> En <sub>80</sub>	1820	0.5	gl
524-3	Fo <sub>20</sub> En <sub>80</sub>	1810	1	fo + en
504-4	An <sub>80</sub> En <sub>20</sub>	1620	6	gl + co
507-3	An <sub>60</sub> En <sub>40</sub>	1590	6	gl
504-5	An <sub>60</sub> En <sub>40</sub>	1570	6	gl + gt
504-3	An <sub>40</sub> En <sub>60</sub>	1660	6	gl
504-2	An <sub>40</sub> En <sub>60</sub>	1640	11	gl + en + (di) + (en)
518-4	An <sub>20</sub> En <sub>80</sub>	1760	4	gl
508-1	An <sub>20</sub> En <sub>80</sub>	1740	6	gl + en + (di) + (en)
503-4	GS-0	1620	7	gl
503-3	GS-0	1600	6	gl + gt + gt
510-1	GS-1	1640	6	gl
515-1	GS-1	1620	8	gl + en + (di) + (en)
513-2	GS-1	1600	6	gl + en + gt + (di)
518-1	GS-1	1580	6	gl + en + gt + (di)
527-3	GS-3	1510	24	gl + qz
517-4	GS-6	1520	24	gl
516-5	GS-6	1500	24	gl + qz + ky
512-1	GS-11	1560	6	gl
509-1	GS-11	1540	6	gl + gt
527-1	AFQ-20	1520	24	gl
528-1	AFQ-20	1500	24	gl + gt + qz
517-1	AFQ-20	1480	24	gl + gt + qz
516-1	AFQ-20	1440	20	gl + gt + qz + ky
503-8	AFQ-22	1630	6	gl + (di)
504-8	AFQ-22	1610	6	gl + en + (di)
503-7	AFQ-22	1590	7	gl + en + gt + (di)
513-3	AFQ-23	1520	6	gl
515-4	AFQ-23	1510	7	gl + qz + ky
512-2	AFQ-23	1500	6	gl + qz + ky
511-1	AFQ-24	1520	6	gl
514-1	AFQ-24	1480	11	gl + co
503-11	AFQ-25	1580	6	gl
503-10	AFQ-25	1560	7	gl + co
524-1	AFQ-26	1580	24	gl

Table 3: continued

Run	Mixture*	T (°C)	Time (h)	Phases
520-2	AFQ-26	1560	26	gl + co
515-2	AFQ-26	1520	8	gl + ky + co
508-3	AFQ-28	1580	6	gl + co
520-1	AFQ-30	1660	6	gl
516-3	AFQ-30	1640	6	gl + sp + (di)
513-1	AFQ-30	1620	6	gl + fo + sp + (di)
511-3	AFQ-30	1580	6	gl + en + di
520-3	AFQ-31	1660	6	gl
516-2	AFQ-31	1640	6	gl + fo + (fo)
514-3	AFQ-31	1600	9	gl + fo + en + (di)
524-4	AFQ-32	1600	6	gl
520-4	AFQ-32	1580	6	gl + sp + (di)
519-4	AFQ-32	1540	6	gl + gt + sp + (di)
517-2	AFQ-32	1500	6	gl + gt + sp + co
517-3	AFQ-33	1440	12	gl + co + (gt)
524-2	AFQ-34	1560	24	gl
528-2	AFQ-34	1540	24	gl + en + (di)
527-2	AFQ-34	1520	24	gl + en + gt + (di)
529-1	AFQ-35	1620	6	gl + (di)
527-4	AFQ-35	1600	7	gl + fo + en + sp + (di)
528-3	AFQ-35	1580	6	gl + en + gt + sp + (di)
532-1	AFQ-36	1540	24	gl + en
531-3	AFQ-36	1520	24	gl + en + gt
560-2	DFA-4	1680	2	gl + fo + di + (fo) + (di)
549-1	DFA-18	1560	21	gl + co
547-4	DFA-24	1610	8	gl + sp + (di)
546-2	DFA-24	1590	6	gl + sp + di + sa + (di)
544-2	DFA-24	1550	7	gl + sp + di + sa + (di)
551-1	DFA-31	1610	8	gl + sp + (di)
547-3	DFA-32	1600	8	gl + fo + (di)
551-4	DEA-1	1545	10	gl
555-4	DEA-1	1540	9	gl + di + gt + (di)
546-1	DEA-2	1500	24	gl + co
554-4	DEA-3	1540	24	gl + (di)
551-2	DEA-3	1520	9	gl + di + co
550-4	DEA-25	1580	9	gl + en + (di)
548-4	DEA-25	1550	8	gl + en + di + gt + (di)
561-3	DEA-29	1560	10	gl + (di)
558-3	DEA-29	1570	8	gl + en + (di)
557-1	DEA-29	1550	8	gl + di + gt + (di)
533-2	CMAS-7	1560	6	gl
545-2	CMAS-7	1550	7	gl + di
543-2	CMAS-7	1545	20	gl + di + gt + (di)
553-4	DEG-24	1635	6	gl
548-2	DEG-24	1630	8	gl + en + (di)
546-3	DEG-24	1600	8	gl + fo + en + (di)
552-3	DEG-24	1575	8	gl + en + di + gt + (di)

Run	Mixture*	T (°C)	Time (h)	Phases
556-4	DEG-26	1580	9	gl + (di)
557-3	DEG-26	1580	8	gl + en + gt + (di)
553-3	DEG-26	1575	8	gl + di + gt + (di)
560-1	DEG-27	1600	8	gl + en + (di)
554-2	DEG-27	1580	8	gl + di + en + (di)
556-3	DEG-27	1575	8	gl + di + gt + (di)
558-4	DEG-28	1590	12	gl + en + (di)
557-2	DEG-28	1575	8	gl + fo + en + (di)
563-2	DEG-28	1560	8	gl + di + gt + (di)
560-4	DEG-28	1550	8	gl + en + di + gt + (di)
561-4	DEG-32	1595	8	gl + en + (di)
567-2	DEG-32	1590	21	gl + en + (di)
562-4	DEG-32	1585	8	gl + fo + en + di + sp + (di)
559-2	DEG-32	1575	8	gl + en + di + gt + (di)
561-2	DEG-32	1550	8	di + gt
567-1	DEG-33	1590	21	gl + (di)
565-2	DEG-33	1585	17	gl + en + di + gt + sp + (di)
565-1	DEG-33	1580	16	gl + di + gt + sp + (di)
564-2	DEG-33	1575	8	di + gt + sp
564-3	DEG-34	1590	8	gl + en + (di)
532-2	CMAS-4	1545	10	gl
533-1	CMAS-4	1525	6	gl + di
530-2	CMAS-4	1505	6	gl + di + gt
539-2	CMAS-5	1560	6	gl
552-2	CMAS-5	1555	10	gl + di + gt + (di)
550-3	CMAS-6	1645	8	gl + fo + (fo) + (di)
546-4	CMAS-6	1650	9	gl + fo + en + (di)
544-1	CMAS-6	1640	6	gl + fo + en + sp + (di)
541-3	CMAS-6	1600	6	gl + fo + en + di + sp + (di)
542-3	CMAS-8	1610	9	gl + (di)
543-3	CMAS-8	1610	7	gl + fo + (fo) + (di)
540-3	CMAS-8	1600	10	gl + fo + en + di + sp + (di)
537-4	CMAS-8	1580	6	gl + fo + en + di + gt + (di)
553-1	CMAS-8	1575	8	fo + en + di + gt + sp
533-3	CMAS-10	1515	6	gl + (di)
535-2	CMAS-10	1500	6	gl + di + (di)
531-1	CMAS-10	1480	6	gl + di + gt + (di)
536-4	CMAS-11	1545	6	gl
535-1	CMAS-11	1525	6	gl + di + (di)
541-1	CMAS-12	1480	24	gl
538-3	CMAS-12	1460	24	gl + gt
536-1	CMAS-12	1420	24	gl + gt + qz
558-2	CMAS-12	1400	32	gl + gt + qz + di + ky + (di)
541-4	CMAS-17	1570	8	gl + (di)
552-1	CMAS-17	1565	8	gl + di + gt + (di)
545-4	CMAS-18	1550	8	gl
549-2	CMAS-18	1545	8	gl + di + gt + (di)
544-4	CMAS-20	1560	7	gl + (di)
550-2	CMAS-20	1555	6	gl + di + gt + (di)

Run	Mixture*	T (°C)	Time (h)	Phases
547-1	CMAS-21	1520	6	gl
540-1	CMAS-21	1500	6	gl + gt + (di)
535-3	CMAS-22	1535	6	gl
537-2	CMAS-22	1515	9	gl + gt
534-2	CMAS-22	1500	6	gl + di + gt + (di)
545-1	DAFQ-23	1585	6	gl + (di)
542-2	DAFQ-23	1580	7	gl + fo + di + gt + sp + (di)
555-1	DAFQ-23	1575	8	gl + fo + en + di + gt + sp + (di)
562-1	DAFQ-23	1575	72	gl + fo + en + di + gt + sp + (di)
549-4	DAFQ-23	1570	8	gl + fo + en + di + gt + sp + (di)
540-2	DAFQ-23	1560	6	en + di + gt + sp
561-1	DAFQ-30	1575	8	gl + fo + (di)
563-4	DAFQ-30	1565	8	gl + fo + en + di + sp + (di)
563-1	DAFQ-31	1500	30	gl + di + gt + (di)
559-1	DAFQ-31	1450	29	gl + di + gt + qz + (di)
518-2	AFQ-30	1560	6	gl + fo + en + di + gt + sp
531-2	AFQ-30	1560	24	gl + fo + en + di + gt + sp

\*For example, the designation An<sub>95</sub> Fo<sub>5</sub> indicates the composition 95% CaAl<sub>2</sub>Si<sub>2</sub>O<sub>8</sub>, 5% Mg<sub>2</sub>SiO<sub>4</sub>, in wt %. (See Table 1 for compositions of mixtures labeled differently.)  
Phase abbreviations: fo, forsterite; qz, quartz; en, enstatite; di, diopside; gt, garnet; sp, spinel; ky, kyanite; co, corundum; sa, sapphirine; gl, glass. Parentheses indicate phases produced during quenching.

*et al.*, 1978). However, the lower pressure trend of expansion of the spinel field relative to the forsterite field is essentially arrested in the pressure interval 2.0–3.0 GPa.

### Diopside–anorthite–enstatite

Figure 6 shows the liquidus surface of the Di–An–En join. It is based on Fig. 2 for the An–En base, experiments on six mixtures (Table 3) within the ternary join, and interpolation between the data of Kushiro (1969, 1972) at 1 atm and 2.0 GPa and Weng & Presnall (1995) at 5.0 GPa along the Di–En side.

The interpolated diopside–enstatite liquidus boundary on the Di–En side is placed at 55 wt % CaMgSi<sub>2</sub>O<sub>6</sub>, which is in disagreement with the position of 38 wt % reported by Davis & Boyd (1966) at 3.0 GPa. Acceptance of the diopside–enstatite boundary of Davis & Boyd (1966) would require a very sharp reduction in the size of the enstatite field as pressure increases from 2.0 to 3.0 GPa, a rate of change so steep, if continued, that the enstatite liquidus field would disappear from the diopside–enstatite join at <4 GPa. Because of this problem and the fact that the data of Kushiro (1969, 1972) and Weng & Presnall (1995) show a smoothly varying and consistent

change in position with increasing pressure, we prefer the interpolated position rather than the directly determined position of Davis & Boyd (1966). We note, however, that our disagreement with the enstatite–diopside liquidus boundary of Davis & Boyd (1966) is unrelated to their location of two-pyroxene subsolidus phase boundaries, which is the main focus of their paper.

### Diopside–enstatite–garnet (Py<sub>2</sub>Gr)

The portion of the aluminous pyroxene plane, MgSiO<sub>3</sub>–CaSiO<sub>3</sub>–Al<sub>2</sub>O<sub>3</sub>, that cuts through the Di–An–Fo–Qz tetrahedron (Fig. 1) is the join CaMgSi<sub>2</sub>O<sub>6</sub>–MgSiO<sub>3</sub>–CaMg<sub>2</sub>Al<sub>2</sub>Si<sub>3</sub>O<sub>12</sub> (Di–En–Py<sub>2</sub>Gr). Figure 7 shows the liquidus surface of this join based on Fig. 2 for the En–Py<sub>2</sub>Gr join, the location discussed above for the diopside–enstatite boundary in the Di–En system, and data for seven mixtures within the join. The garnet field is shown as an extremely narrow wedge that just barely intersects the join. None of the mixtures on this join show garnet as the sole primary phase; but one mixture, DEG-26, shows garnet and enstatite simultaneously appearing at the liquidus (Table 3). Also, we have analyzed the glass in equilibrium with forsterite, enstatite, diopside, garnet, and spinel in run 562-1 (an

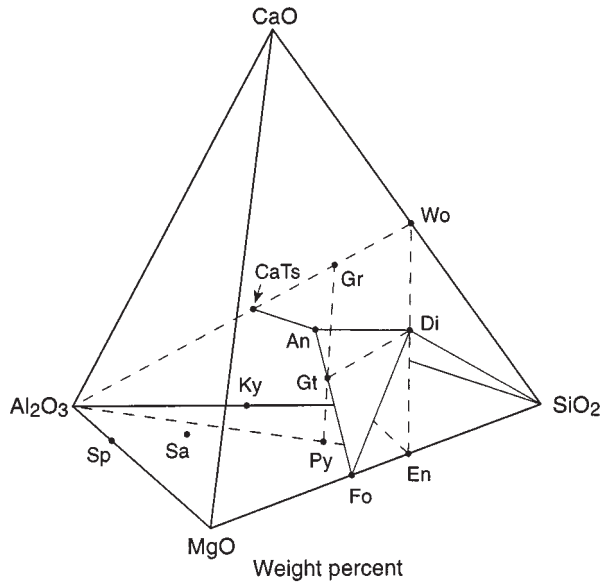


**Fig. 1.** The tetrahedron CaO–MgO–Al<sub>2</sub>O<sub>3</sub>–SiO<sub>2</sub>, showing the simplified tholeiitic basalt tetrahedron Di–Fo–An–Qz. The aluminous pyroxene plane (MgSiO<sub>3</sub>–CaSiO<sub>3</sub>–Al<sub>2</sub>O<sub>3</sub>) and lines lying in this plane are dashed. An, anorthite (CaAl<sub>2</sub>Si<sub>2</sub>O<sub>8</sub>); CaTs, Ca Tschermak's molecule (CaAl<sub>2</sub>SiO<sub>6</sub>); Di, diopside (CaMgSi<sub>2</sub>O<sub>6</sub>); En, enstatite (MgSiO<sub>3</sub>); Fo, forsterite (Mg<sub>2</sub>SiO<sub>4</sub>); Gt, garnet (CaMg<sub>2</sub>Al<sub>2</sub>Si<sub>3</sub>O<sub>12</sub>); Gr, grossular (Ca<sub>3</sub>Al<sub>2</sub>Si<sub>3</sub>O<sub>12</sub>); Py, pyrope (Mg<sub>3</sub>Al<sub>2</sub>Si<sub>3</sub>O<sub>12</sub>); Sp, spinel (MgAl<sub>2</sub>O<sub>4</sub>); Wo, wollastonite (CaSiO<sub>3</sub>); Ky, kyanite (Al<sub>2</sub>SiO<sub>5</sub>); Sa, sapphirine (Mg<sub>2</sub>Al<sub>4</sub>Si<sub>10</sub>).

*Table 4: Piercing points on An–Fo–Qz face*

Phases	Liquid comp. (wt %)	<i>T</i> (°C)
fo + en + sp + liq	An <sub>48</sub> Fo <sub>45</sub> Qz <sub>7</sub>	1635
gt + en + sp + liq	An <sub>51</sub> Fo <sub>41</sub> Qz <sub>8</sub>	1625
gt + en + qz + liq	An <sub>53</sub> Fo <sub>21</sub> Qz <sub>26</sub>	1525
gt + co + sp + liq	An <sub>68</sub> Fo <sub>23</sub> Qz <sub>9</sub>	1545
gt + co + ky + liq	An <sub>63</sub> Fo <sub>14.5</sub> Qz <sub>22.5</sub>	1480
gt + qz + ky + liq	An <sub>60</sub> Fo <sub>15</sub> Qz <sub>25</sub>	1440
co + qz + ky + liq	An <sub>68</sub> Fo <sub>5</sub> Qz <sub>27</sub>	1520

Phase abbreviations as in Table 3.

invariant assemblage in pressure–temperature space), and the composition of this glass lies slightly to the forsterite side of the Di–En–Py<sub>2</sub>Gr plane (Fig. 1 and Table 5). This means that the garnet volume in the Di–An–Fo–Qz tetrahedron just barely penetrates into the forsterite-rich side of the Di–En–Py<sub>2</sub>Gr plane. The triangle in Fig. 7 shows the position of the glass analysis as projected from Fo. If the garnet volume were restricted to the SiO<sub>2</sub>-rich side of the plane, then the forsterite volume would

necessarily penetrate the plane from the forsterite-rich side. Mixture DEG-33 shows enstatite, diopside, garnet, and spinel simultaneously appearing at the liquidus, but not forsterite (Table 3). Because DEG-33 is almost coincident with the projected position of the invariant point (Fig. 7), forsterite would be expected as part of the assemblage if the forsterite volume were extended to the SiO<sub>2</sub>-rich side of the plane. Even though all of these data consistently indicate that the garnet volume just barely penetrates the aluminous pyroxene plane, the analytical and experimental uncertainties are sufficiently large that we cannot be completely certain of this conclusion. However, we assume in the remaining discussion that a very small penetration occurs.

Figure 7 shows the Di–En–Py<sub>2</sub>Gr diagram in an orientation that allows easy comparison with Fig. 1 and later figures illustrating phase relations in the Di–An–Fo–Qz tetrahedron. The more conventional orientation for the aluminous pyroxene plane is shown in Fig. 8, which is a reoriented version of Fig. 7 expanded to include the composition of pyrope. Here the spinel–enstatite boundary is extended to the MgSiO<sub>3</sub>–Mg<sub>3</sub>Al<sub>2</sub>Si<sub>3</sub>O<sub>12</sub> side. Also shown are the compositions of diopside, enstatite, and garnet in equilibrium with liquid at the open triangle (Tables 5 and 6, run 562-1). Figure 8 allows a comparison with the data of Kushiro & Yoder (1974) at 2.0 GPa and with three studies at 3.0 GPa, the CaMgSi<sub>2</sub>O<sub>6</sub>–Mg<sub>3</sub>Al<sub>2</sub>Si<sub>3</sub>O<sub>12</sub> join (O'Hara, 1963; O'Hara & Yoder, 1967), the MgSiO<sub>3</sub>–Mg<sub>3</sub>Al<sub>2</sub>Si<sub>3</sub>O<sub>12</sub> system (Boyd & England, 1964), and the Ca<sub>3</sub>Al<sub>2</sub>Si<sub>3</sub>O<sub>12</sub>–Mg<sub>3</sub>Al<sub>2</sub>Si<sub>3</sub>O<sub>12</sub> system (Maaløe & Wyllie, 1979). Our data are consistent with the 2.0 GPa data of Kushiro & Yoder (1974) on the aluminous pyroxene join. Also, we find consistency with the 3.0 GPa data of Boyd & England (1964) and Maaløe & Wyllie (1979) where direct overlap occurs. However, our liquidus boundaries are significantly different from those given by O'Hara & Yoder (1967) for the CaMgSi<sub>2</sub>O<sub>6</sub>–Mg<sub>3</sub>Al<sub>2</sub>Si<sub>3</sub>O<sub>12</sub> join. They show a garnet field straddling the area where we have drawn the spinel–enstatite boundary line and their diopside field is larger than ours. We are not certain of the reason for these differences, but it is possible that the run durations in the early study of O'Hara & Yoder (1967) were not long enough to attain equilibrium.

Maaløe & Wyllie (1979, fig. 1) show a small pyrope liquidus field roughly at the midpoint of the pyrope–grossular join. Although this field is outside the range of our liquidus data, its existence is in conflict with our data showing only a very small penetration of the garnet volume through the aluminous pyroxene plane (Figs 7 and 8). The existence of the garnet field in the study of Maaløe & Wyllie is based on one run at 1550°C for the mixture, 50% pyrope, 50% grossular; this contains garnet, quench diopside, and glass (their fig. 1). If the quench

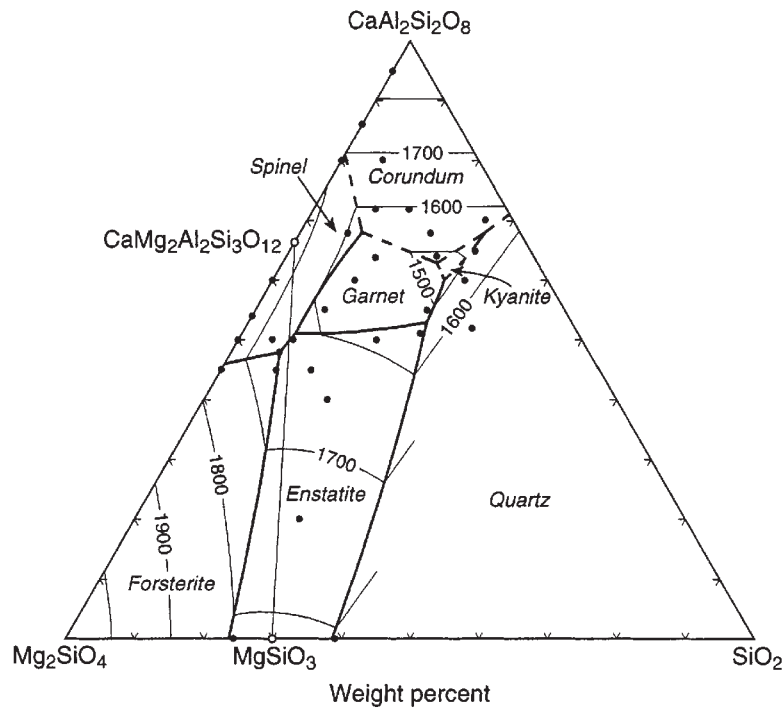


**Fig. 2.** Liquidus surface for the join  $\text{CaAl}_2\text{Si}_2\text{O}_8$ – $\text{Mg}_2\text{SiO}_4$ – $\text{SiO}_2$  (An–Fo–Qz) at 3.0 GPa. The melting temperature of An is interpolated from Lindsley (1968) and that of Fo is from Davis & England (1964). Filled circles are compositions of starting mixtures. Bold lines (dashed where inferred) are boundary lines and fine lines are liquidus isotherms with temperatures in °C. Italicized labels identify liquidus primary phase fields. The line from  $\text{CaMg}_2\text{Al}_2\text{Si}_3\text{O}_{12}$  to  $\text{MgSiO}_3$  is the trace of the aluminous pyroxene thermal divide.

diopside were interpreted instead to be equilibrium diopside, the liquidus could be drawn so as to join the spinel and diopside fields and omit the garnet liquidus field. Such a diagram would be consistent with the position of the diopside–spinel boundary surface that we find [compare fig. 1 of Maaløe & Wyllie (1979) with our Figs 1, 5, and 9]. Their observation of garnet below the liquidus at 1550°C would also be consistent with temperatures at which we find garnet. This interpretation of the results of Maaløe & Wyllie (1979) is supported by the study of the pyrope–grossular join at 3.0 GPa by Malinovskii *et al.* (1976), who joined the fields of spinel and diopside at the liquidus and found garnet below the liquidus at 1550°C.

### Diopside–anorthite–forsterite–quartz

Figure 9 shows the arrangement of primary phase volumes in the Di–An–Fo–Qz tetrahedron. The An–Fo–Qz base is from Fig. 2 and the left-hand face, Di–An–Fo, is from Fig. 5. Phase boundaries on the back face, Di–An–Qz, are extrapolated from the data of Clark *et al.* (1962) at 2.0 GPa and are poorly constrained. We draw the quaternary phase relations so that the kyanite volume does not extend to the back face, but this is uncertain.

Positions of phase boundaries within the tetrahedron are controlled by Figs 6 and 7, and by data on 15 additional mixtures not lying on a specific join (Tables 3, 5, and 6). Compositions of the invariant points are given in Table 7. The location of point Y is not well constrained but must lie within the tetrahedron. It has been placed roughly halfway between the left-hand face of the tetrahedron and points X and W. Similarly, the position of point Z is constrained only to lie somewhere between the base of the tetrahedron and the vicinity of point W. Point N has been placed within the tetrahedron, but may lie outside the tetrahedron if the kyanite volume extends through the back face, Di–An–Qz. The back face has not been studied. The positions of points H, L, W, and X are reasonably well constrained by the data in Tables 3 and 5.

Two points, P (ol + en + di + sp + gt + liq, run 562-1, Table 5) and M (gt + di + ky + qz + liq, run 558-2, Table 5) have been determined by microprobe analysis of glass in equilibrium with all the crystalline phases at the invariant point (see analyses of crystalline phases in Table 6). Using the phase compositions at M, we have calculated the defining reaction for point M (Table 8). Presnall (1991) deduced a rule that allows the direction of decreasing temperature along liquidus univariant lines to be determined from the reaction that defines the

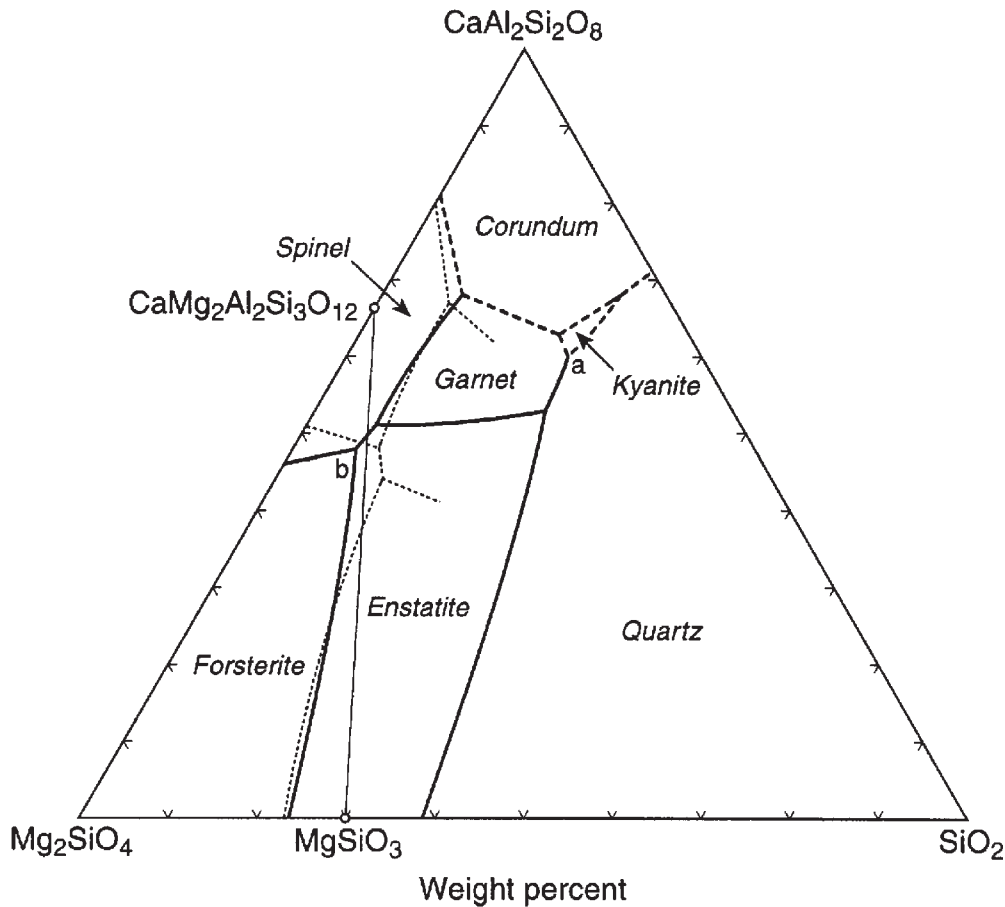


**Fig. 3.** Comparison of liquidus phase relations determined in this study with those of Adam (1988) at 2.8 GPa. Bold lines are boundary lines from this study and fine dashed lines are boundary lines from Adam (1988).

isobaric invariant point. This rule states that liquidus univariant lines that decrease in temperature away from an invariant point must contain the entire mineral assemblage found on the opposite side of the reaction from the liquid (assuming that the reaction is written so that all coefficients are positive). All other univariant lines must decrease in temperature toward the invariant point. Using this rule, we find that the line along which kyanite, quartz, and diopside are in equilibrium decreases in temperature away from point M. All other liquidus univariant lines decrease in temperature toward M.

Point P is of particular interest. This liquid, previously discussed in relation to Figs 7 and 8, is in equilibrium with olivine, enstatite, diopside, spinel, and garnet. Thus, P is an invariant point in pressure-temperature space and is of considerable petrologic importance because it marks the transition, at the solidus, between model spinel lherzolite and garnet lherzolite. By chance, our choice of 3.0 GPa for this study coincides with the pressure of this invariant point. This explains the fact that six isobaric univariant lines involving a liquid phase emanate from

P (Fig. 9) rather than four, as is the case for all the other points, which are merely isobarically invariant.

Tables 5 and 6 show the compositions of all six phases in equilibrium at point P, and we emphasize that all the phases are analyzed from a single experiment (562-1, Table 3) of 72 h duration. From these data, we have calculated reaction coefficients for each of the pressure-temperature univariant lines just as they emanate from the invariant point (Table 8). The corresponding Schreinemakers construction showing the arrangement of univariant lines around the invariant point is given in Fig. 10. The reactions of interest for model lherzolite, shown as bold lines, are the garnet-absent reaction, (Gt), for melting of spinel lherzolite, the spinel-absent reaction, (Sp), for melting of garnet lherzolite, and the reaction defining the transition between spinel lherzolite and garnet lherzolite, (Liq). Reaction coefficients for melting along the univariant lines (Gt) and (Sp) will change at pressures higher and lower than 3.0 GPa, and these changes have been given by Gudfinnsson & Presnall (1996). For (Sp) at pressures above that of point P,

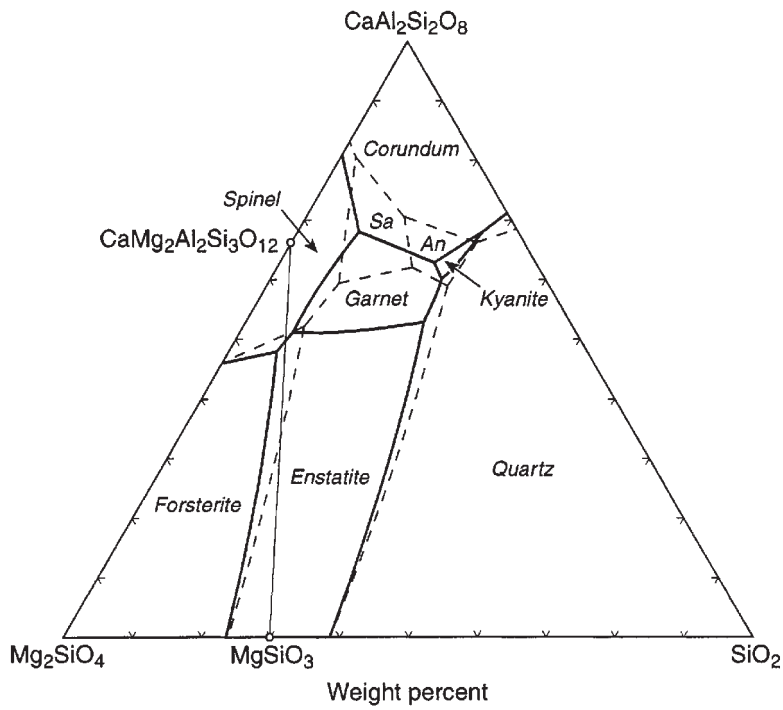


**Fig. 4.** Comparison of liquidus phase relations determined in this study with those of Liu & Presnall (1990) at 2.0 GPa. Bold lines and fine dashed lines are boundary lines at 3.0 and 2.0 GPa, respectively. Abbreviations as in Fig. 1.

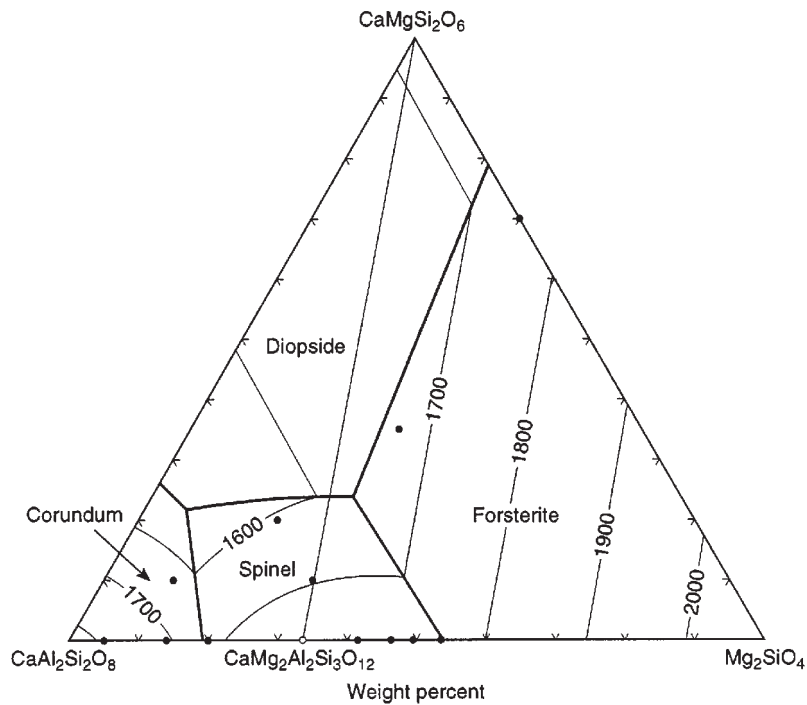


**Fig. 5.** Liquidus surface of the join  $\text{CaMgSi}_2\text{O}_6$ - $\text{CaAl}_2\text{Si}_2\text{O}_8$ - $\text{Mg}_2\text{SiO}_4$  at 3.0 GPa. Filled circles are starting mixtures. Bold lines are boundary lines and fine lines are liquidus isotherms in  $^\circ\text{C}$ . The line from  $\text{CaMg}_2\text{Al}_2\text{Si}_3\text{O}_{12}$  to  $\text{CaMgSi}_2\text{O}_6$  is the trace of the aluminous pyroxene thermal divide.

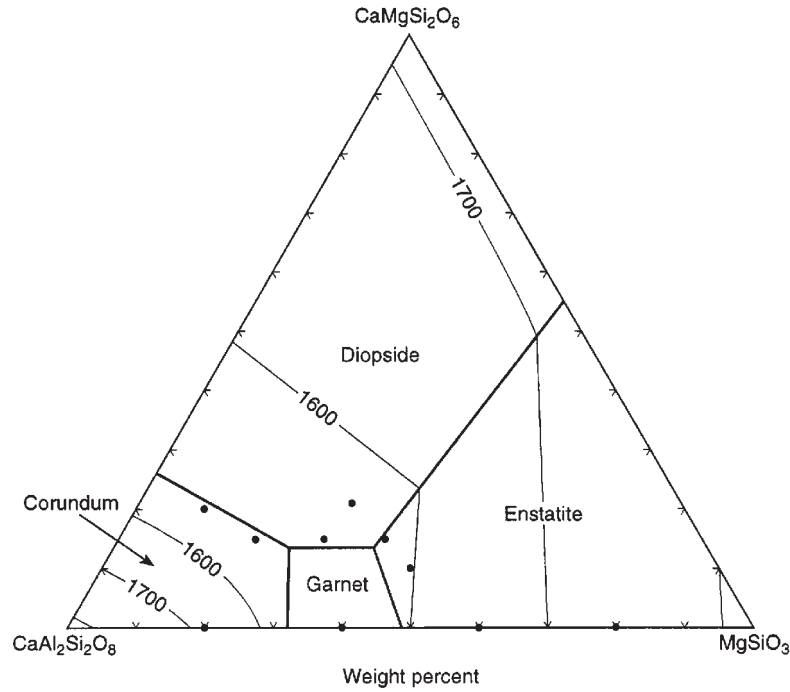


Fig. 6. Liquidus surface of the join  $\text{CaMgSi}_2\text{O}_6$ - $\text{CaAl}_2\text{Si}_2\text{O}_8$ - $\text{MgSiO}_3$  at 3.0 GPa. Lines and symbols as in Fig. 5.

Table 5: Compositions of glasses (wt %)

Run:	562-1	558-2	565-1	548-4	559-1	544-2
Mixture:	DAFQ-23	CMAS-12	DEG-33	DEA-25	DAFQ-31	DFA-24
Phases:	fo, en, gt, di, sp, liq	di, gt, qz, ky, liq	di, sp, gt, liq	en, di, gt, liq	di, gt, qz, liq	di, sp, sa, liq
Points:	11	3	19	7	4	2
SiO <sub>2</sub>	47.3 (0.4)	55.7 (0.1)	47.4 (0.4)	53.3 (0.3)	58.4 (0.4)	45.9 (1.0)
Al <sub>2</sub> O <sub>3</sub>	17.0 (0.2)	22.6 (0.2)	18.0 (0.2)	18.5 (0.2)	20.0 (0.1)	21.8 (1.2)
MgO	22.1 (0.2)	6.4 (0.1)	21.2 (0.1)	15.0 (0.2)	8.6 (0.1)	14.2 (1.3)
CaO	13.5 (0.2)	14.4 (0.1)	13.3 (0.5)	13.5 (0.2)	13.4 (0.1)	16.1 (1.1)
Total	99.9 (0.4)	99.1 (0.5)	99.9 (0.5)	100.3 (0.4)	100.4 (0.3)	97.9 (0.3)
An	46.4	62.2	49.2	50.3	54.3	60.7
Di	16.0	7.8	13.1	12.7	9.4	16.1
Fo	33.5	8.8	32.7	22.0	11.9	20.1
Qz	4.2	21.2	5.0	15.0	24.4	3.2
Py <sub>2</sub> Gr	69.8		74.1			
Di	16.0		13.1			
En	13.9		11.2			
Fo	0.2					
Qz			1.6			

Phase abbreviations as in Table 3. Parentheses indicate two standard deviations.

Table 6: Mineral compositions (wt %)

Run:	562-1				558-2		544-2	
Mixture:	DAFQ-23				CMAS-12		DFA-24	
Phases:	fo, en, di, gt, sp, liq				di, gt, qz, ky, liq		di, sp, sa, liq	
Mineral:	Ol	En	Di	Gt	Di	Gt	Di	Sa
Points:	10	10	15	14	10	10	1	1
SiO <sub>2</sub>	42.8 (0.4)	53.6 (0.1)	51.4 (0.7)	44.2 (0.3)	47.7 (0.3)	43.8 (0.3)	45.8	18.5
Al <sub>2</sub> O <sub>3</sub>		10.6 (0.1)	10.9 (1.0)	25.2 (0.2)	19.3 (0.4)	25.3 (0.4)	19.3	58.5
MgO	56.8 (0.6)	32.9 (0.1)	23.7 (0.6)	25.2 (0.3)	12.1 (0.4)	22.5 (0.4)	15.1	23.2
CaO	0.33 (0.04)	2.83 (0.03)	13.8 (0.6)	5.4 (0.1)	21.0 (0.3)	8.4 (0.2)	20.4	0.7
Total	99.9 (0.5)	99.9 (0.1)	99.8 (0.3)	100.0 (0.3)	100.1 (0.5)	100.0 (0.4)	100.6	100.9
<i>Cations on the basis of N oxygens</i>								
N	4	6	6	24	6	24	6	10
Si	1.003	1.807	1.790	6.018	1.683	6.009	1.614	1.054
Al <sup>IV</sup>		0.193	0.210		0.317		0.386	3.920
Al <sup>VI</sup>		0.227	0.238	4.043	0.486	4.090	0.418	
Mg	1.986	1.653	1.233	5.107	0.635	4.606	0.794	1.969
Ca	0.008	0.102	0.515	0.791	0.794	1.240	0.772	0.043
Total	2.997	3.982	3.986	15.959	3.915	15.945	3.984	6.986

Abbreviations as in Table 3. Parentheses indicate two standard deviations.

enstatite is the only phase in reaction relationship with the liquid. For (Gt) at pressures below that of point P, both enstatite and forsterite are in reaction relationship with the liquid, but this changes at some pressure between 3.0 and 2.8 GPa. Gudfinnsson & Presnall (1996) found that at lower pressures, only forsterite is in reaction relationship, in agreement with Kushiro & Yoder (1974). Therefore, as discussed by Gudfinnsson & Presnall (1996), a singular point must exist for (Gt) between 3.0 and 2.8 GPa. Also, the reaction coefficient for En in the (Gt) reaction (Table 8) is extremely small, which is consistent with transfer of En to the other side of the equation at a pressure not far below 3.0 GPa.

The location of point P at 3.0 GPa is based on five different experiments, in each of which six phases were found at temperatures of 1560°C, 1560°C, 1570°C, 1575°C, and 1575°C (Table 3, runs 518-2, 531-2, 562-1, 555-1, and 549-4). On the basis of these runs, the temperature of point P is taken to be  $1568 \pm 10^\circ\text{C}$ . Run 562-1 was chosen for analyses of the coexisting phases because of its long duration. Even though all the experiments were done at a nominal pressure of 3.0 GPa, uncertainties in the pressure were large enough that phase assemblages that define four of the five  $P$ - $T$  univariant lines (Fig. 10) emanating from point P were observed. These are the phase assemblages fo + en + di + sp + liq (Table 3, runs 540-3, 562-4, 541-3, 563-4) and en + di + sp + gt + liq (Table 3, run

565-2), which occur at pressures immediately below that of the invariant point, and the phase assemblages fo + en + di + gt + liq (Table 3, run 537-4) and fo + di + sp + gt + liq (Table 3, run 542-2), which occur at pressures immediately above that of the invariant point. Our location of invariant point P is in excellent agreement with the position of the spinel lherzolite to garnet lherzolite subsolidus transition as determined by Jenkins & Newton (1979) (900–1000°C), Gasparik (1984) (1400°C), and O'Hara *et al.* (1971) (their preferred piston-out data at 1400–1500°C).

### Diopside saturation surface

Figures 11 and 12 show the diopside saturation surface projected from CaMgSi<sub>2</sub>O<sub>6</sub>. The most interesting and complex area of the diagram is the upper part in the vicinity of the garnet + diopside surface, and this is also the area where most of our data are concentrated. The perimeter of the garnet + diopside surface is constrained by two glass analyses that define invariant points P and M, three additional glass analyses located on univariant lines, and two points on univariant lines located by phase relations on the diopside–anorthite–enstatite join (Fig. 6). One additional glass analysis in equilibrium with diopside, spinel, and sapphirine provides control on the left-hand side of the sapphirine field.

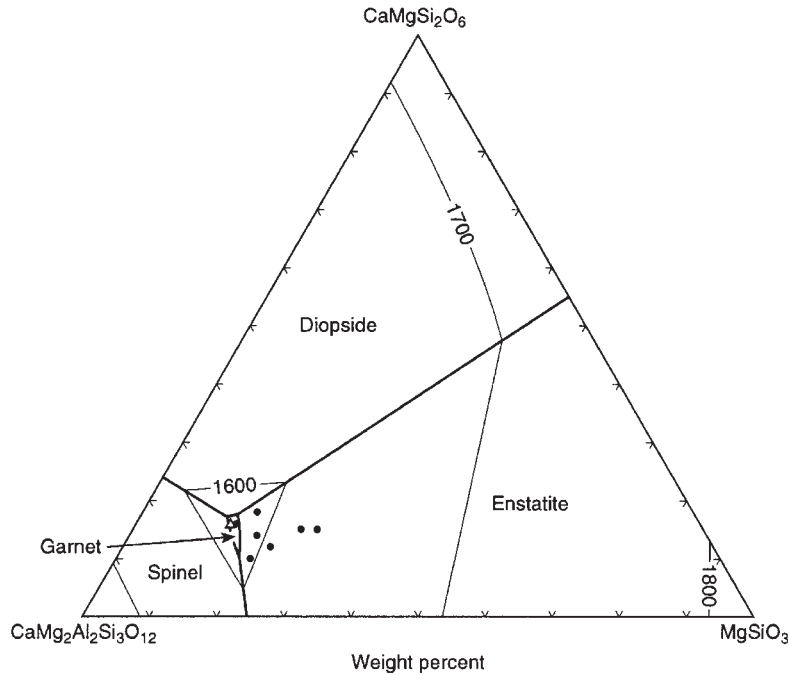


**Fig. 7.** Liquidus surface of the join  $\text{CaMgSi}_2\text{O}_6$ - $\text{CaMg}_2\text{Al}_2\text{Si}_3\text{O}_{12}$ - $\text{MgSiO}_3$  at 3.0 GPa. The triangle is a projection of the composition of liquid P (Figs 7, 9, 11, and 12; Table 5, run 562-1) from Fo. Lines and other symbols as in Fig. 5. The diopside-enstatite, diopside-garnet, and enstatite-garnet boundary lines are ternary. On the diopside-garnet boundary line, temperature decreases to the left.

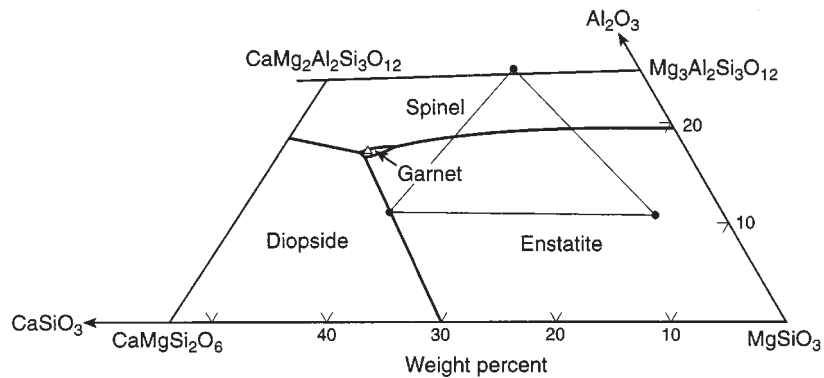


**Fig. 8.** Liquidus phase relations for the join  $\text{CaMgSi}_2\text{O}_6$ - $\text{CaMg}_2\text{Al}_2\text{Si}_3\text{O}_{12}$ - $\text{Mg}_3\text{Al}_2\text{Si}_3\text{O}_{12}$ - $\text{MgSiO}_3$  at 3.0 GPa. Bold lines are liquidus boundary lines. The garnet-diopside, garnet-enstatite, and diopside-enstatite boundary lines are ternary, and, in all three cases, temperature decreases to the left. Fine lines connect coexisting diopside, enstatite, and garnet compositions (Table 6, run 562-1) in equilibrium with liquid P (triangle).

In Fig. 12, directions of decreasing temperature are shown on the univariant lines. For univariant lines radiating from invariant points P and M, these directions are determined by the reactions at the invariant points (Table 8) and the rule deduced by Presnall (1991). This rule requires that the olivine-diopside-spinel line decreases in temperature away from point P. However, we have a determination of the temperature on this line in the left-hand face, Di-An-Fo, that is significantly

higher than the temperature at P. Therefore, a temperature minimum occurs on this line. For the other invariant points, data are insufficient for an accurate determination of reaction coefficients, but directions of decreasing temperature have nevertheless been added based on what we believe to be the form of each reaction. In all cases, directions of decreasing temperature deduced on this criterion are consistent with temperature contours in Fig. 12.

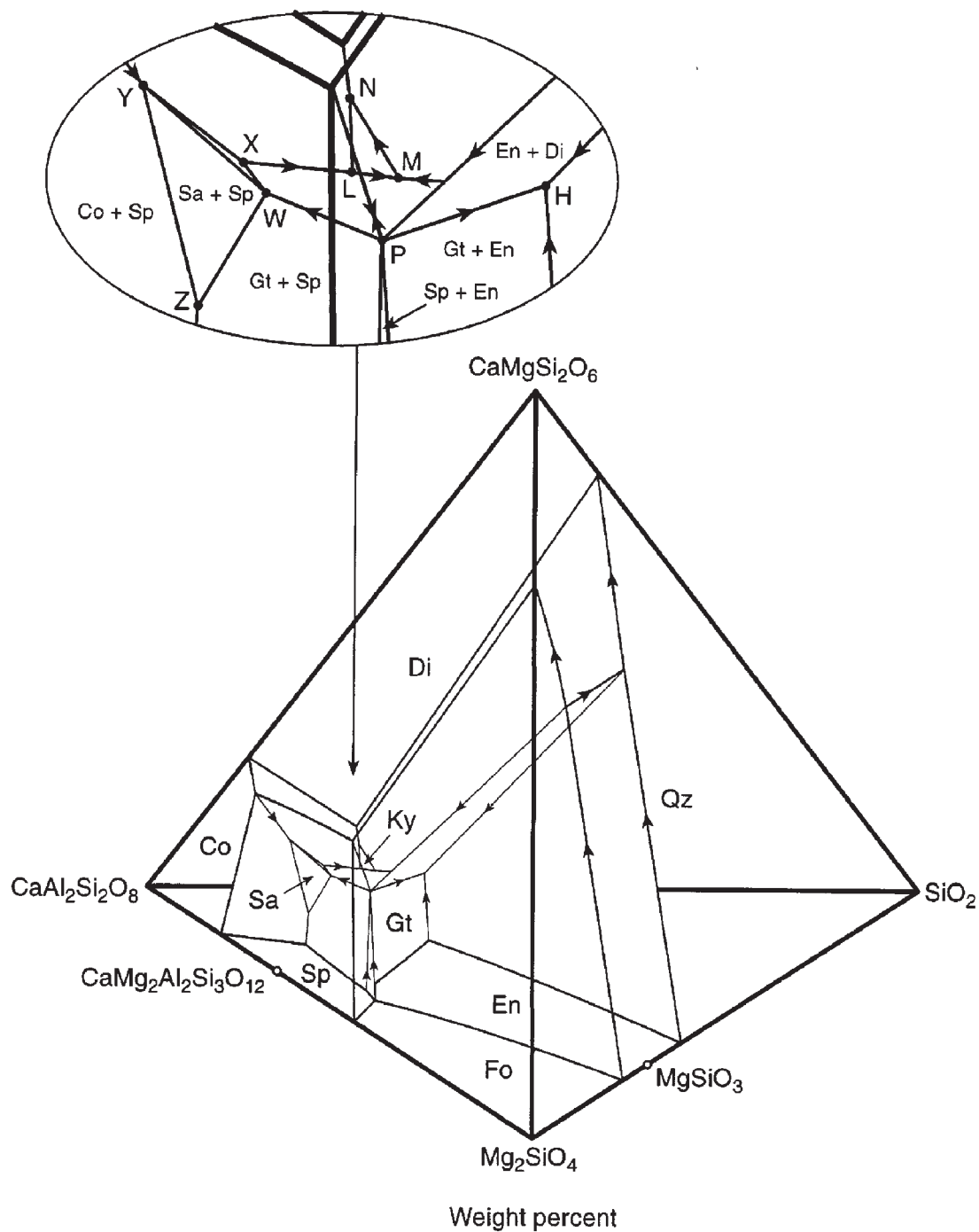


**Fig. 9.** Liquidus phase relations in the system  $\text{CaMgSi}_2\text{O}_6$ - $\text{CaAl}_2\text{Si}_2\text{O}_8$ - $\text{Mg}_2\text{SiO}_4$ - $\text{SiO}_2$  at 3.0 GPa. Arrows show directions of decreasing temperature for strictly ternary or quaternary boundary lines, but these arrows are omitted where uncertainty exists and where lines are crowded. See Figs 12 and 15 for additional arrows not shown here. Capital letters label isobaric invariant points, with the exception that P is a six-phase invariant point in pressure-temperature space. Medium lines are liquidus boundaries in the faces of the tetrahedron. Fine lines are liquidus univariant lines inside the tetrahedron. Abbreviations labeling primary phase volumes are the same as in Fig. 1, with the addition of co for corundum.

Table 7: Invariant point compositions (wt %)

	H*	P	L	M	N	W	X	Y	Z
<i>T</i> (°C):	1460	1568	1410	1400	<1400	1550	1540	1545	
Phases:	en,di,gt, qz,liq	fo,en,di, gt,sp,liq	di,gt,ky, co,liq	di,qz,ky, gt,liq	di,gz,ky, co,liq	di,sp,gt, sa,liq	di,sp,gt, co,liq	di,sp,sa, co,liq	sp,gt,sa, co,liq
SiO <sub>2</sub>	58.3	47.4†	54.8	56.2	55.6	47.4	48.4	46.7	47.6
Al <sub>2</sub> O <sub>3</sub>	19.3	17.0	23.4	22.8	23.5	22.1	21.9	23.7	23.8
MgO	9.3	22.1	6.8	6.5	4.8	15.8	13.8	11.8	14.0
CaO	13.1	13.5	15.0	14.5	16.1	14.7	16.0	17.7	14.6
An	52.8	46.4	63.8	62.2	64.9	57.6	60.6	65.6	64.9
Di	9.5	16.0	8.3	7.8	11.0	14.0	14.0	17.0	6.0
Fo	13.1	33.4	9.1	8.8	4.5	23.2	19.3	15.0	22.5
Qz	24.6	4.2	18.8	21.2	19.6	5.2	6.1	2.4	6.6

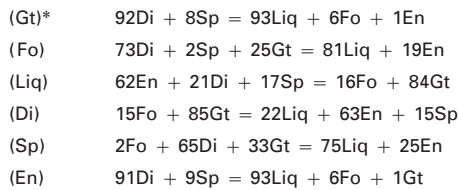
Abbreviations as in Table 3.

\*Letters correspond to labels in Fig. 9.

†For precision of compositions P and M, see Table 5, columns 1 and 2, respectively. For the other compositions, the number of significant figures is unrelated to precision, which varies strongly (see text). The values merely describe the locations of the points in the diagrams.

Table 8: Reactions

Univariant curves that radiate in pressure–temperature space from invariant point *P*



Isobaric invariant point *M*†



\*Mineral names in parentheses label the univariant curves according to the absent phase. Phase composition data are from run 562-1 (Tables 4 and 5). Sp is stoichiometric. The stable parts of the first three reactions are at <3.0 GPa and the stable parts of the last three reactions are at >3.0 GPa (see Fig. 7).

†See Fig. 6. Phase composition data from run 558-2, Tables 4 and 5.

### Spinel lherzolite to garnet lherzolite transition

Figures 13 and 15a (slightly below 3.0 GPa) and Figs 14 and 15b (slightly above 3.0 GPa) show further details about the solidus transition from spinel lherzolite to garnet lherzolite. In these figures, the labels for isobaric invariant points shown in parentheses refer to univariant reactions with the same labels in Fig. 10 and Table 8. Directions of decreasing temperature (Fig. 15) are determined from the reactions at each invariant point (Table 8) and the rule given by Presnall (1991). The

coefficients for these reactions (Table 8) are based on the compositions of phases at point P. As pressure increases from slightly below 3.0 GPa (Fig. 13), the isobaric invariant points (Fo) and (Gt) approach each other and meet at 3.0 GPa to produce the *P–T* invariant point P (Fig. 9). A further increase in pressure produces three new isobaric invariant points, (En), (Sp), and (Di), shown in Fig. 14. Also shown in Fig. 15 (see also Figs 9 and 12) is a temperature minimum on the sp–di–fo univariant line. The temperature maximum on the en–di–gt univariant line is required because all three of these phases

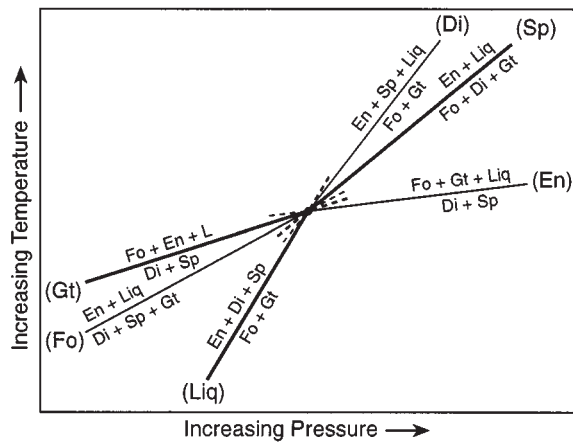


**Fig. 10.** Schematic Schreinemakers construction of univariant lines around the invariant point P (Figs 9, 11, 12, and 15). Phases in parentheses label the univariant curves according to the absent phase (see Table 8). Abbreviations as in Fig. 1.

lie on the aluminous pyroxene plane. Because the separation of invariant point P from the aluminous pyroxene plane is very small, the temperature maximum would not be experimentally resolvable at 3.0 GPa.

**PHASE RELATIONS IN NATURAL VS CMAS COMPOSITIONS**

The applicability of phase relations in simplified model systems to the generation and crystallization of natural magmas is frequently questioned on grounds that important components of natural magmas are missing. Therefore, before proceeding to some petrological applications, the issue of relevance will be addressed. The lherzolite melting reactions in Table 9 show that in the spinel lherzolite field, not only is the form of the melting reaction in the CMAS system identical to that in the CMAS–Na<sub>2</sub>O system and in natural compositions, but the reaction coefficients are also very similar. By this measure, the CMAS system models the melting behavior

of natural compositions very closely despite the absence of such components as FeO, Na<sub>2</sub>O, and Cr<sub>2</sub>O<sub>3</sub>.

An issue of more specific relevance to the present study is the effect of additional components on the pressure of the spinel lherzolite to garnet lherzolite transition at the lherzolite solidus. Walter & Presnall (1994, fig. 4) have shown that 1.5% Na<sub>2</sub>O in the liquid increases the pressure of the transition by ~0.2 GPa. For 10% FeO in the liquid, the pressure of the transition is reduced by ~0.2 GPa (Gudfinnsson, 1995; Gudfinnsson & Presnall, 1995). Thus, the effects of Na<sub>2</sub>O and FeO essentially cancel and broaden the transition from a single point on the solidus to a small transition interval. Other components, taken together, apparently increase the pressure of the transition slightly, because O’Hara *et al.* (1971) found subsolidus transition pressures ~0.2 GPa higher for natural lherzolite than for CMAS lherzolite (see also Jenkins & Newton, 1979; Gasparik, 1984).

In volatile-free natural lherzolite, solidus temperatures are lower than in the CMAS system because of the presence of additional components. Because the spinel lherzolite to garnet lherzolite subsolidus transition has a positive *dT/dP* slope, the pressure of this transition at the volatile-free solidus for natural compositions will be lower than the pressure of 3.0 GPa we have found for the CMAS system. For example, our data combined with those of O’Hara *et al.* (1971) indicate that a temperature decrease of 100°C in the CMAS system to ~1470°C would cause a decrease in the pressure of the transition of ~0.4 GPa. Thus, the combined effects of temperature and a small shift in the pressure of the subsolidus transition suggest that if the transition at the solidus of natural lherzolite occurs at 1470°C, the pressure would be ~2.8 GPa under volatile-free conditions, and that it would occur over a small pressure interval. This estimated location is extremely close to a recent determination of 1450°C, 2.8 GPa (hot piston-out with no pressure correction) for a pyrolite composition (A. Robinson & B. J. Wood, personal communication, 1997). This small shift in the pressure of the solidus transition caused by additional components reinforces our conclusion that

*Table 9: Comparison of lherzolite melting reactions for model systems and natural compositions*

<i>P</i> (GPa)	Melting interval	System	Melting reaction (wt %)	Reference
1.1	Invariant	CMAS	36 opx + 55 cpx + 9 sp = 77 liq + 23 ol	1
1.1	12–22%	CMAS–Na <sub>2</sub> O	34 opx + 56 cpx + 10 sp = 75 liq + 25 ol	2
1.0	<i>mg-no.</i> 75–67	Natural	35 opx + 59 cpx + 5 sp = 78 liq + 22 ol	3
1.0	~7–18%	Natural	31 opx + 58 cpx + 11 sp = 82 liq + 18 ol	4

1, Gudfinnsson & Presnall (1996); 2, Walter *et al.* (1995); 3, Kinzler & Grove (1992); 4, Baker & Stolper (1994).

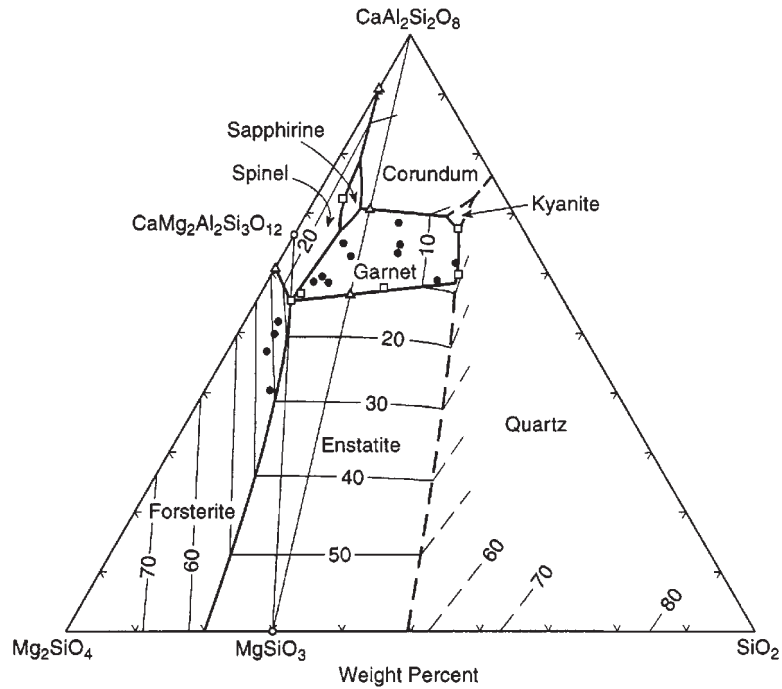


**Fig. 11.** Diopside saturation surface of Fig. 6 projected from  $\text{CaMgSi}_2\text{O}_6$ . For example, the field labeled enstatite shows the projected divariant liquidus boundary surface along which enstatite, diopside, and liquid are in equilibrium. Bold lines are projected univariant boundary lines (dashed where inferred) and fine lines are contours of wt %  $\text{CaMgSi}_2\text{O}_6$ . Filled circles are projected starting compositions. Triangles are locations of boundary lines taken from Figs 5 and 6. Squares are glass compositions from Table 5. The line from  $\text{CaMg}_2\text{Al}_2\text{Si}_3\text{O}_{12}$  to  $\text{MgSiO}_3$  is the trace of the aluminous pyroxene thermal divide.

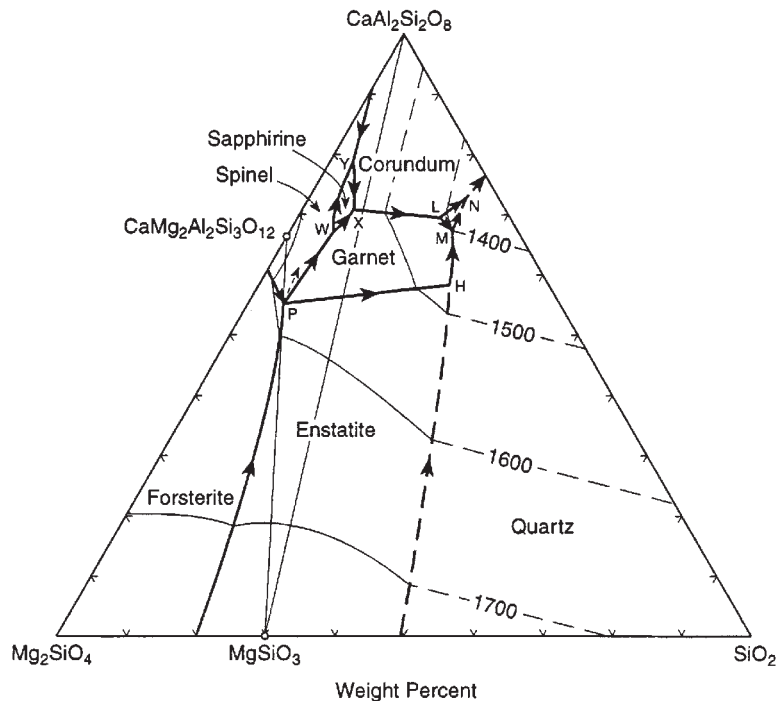


**Fig. 12.** Diopside saturation surface as in Fig. 11, showing temperature contours in  $^{\circ}\text{C}$ . Arrows on boundary lines indicate directions of decreasing temperature. Invariant point labels in capital letters are keyed to Fig. 9. Dashed line extending from point P indicates direction of liquid fractionation path (see text). A temperature minimum exists on the forsterite–spinel–diopside boundary but it is not shown because it lies very close to point P.

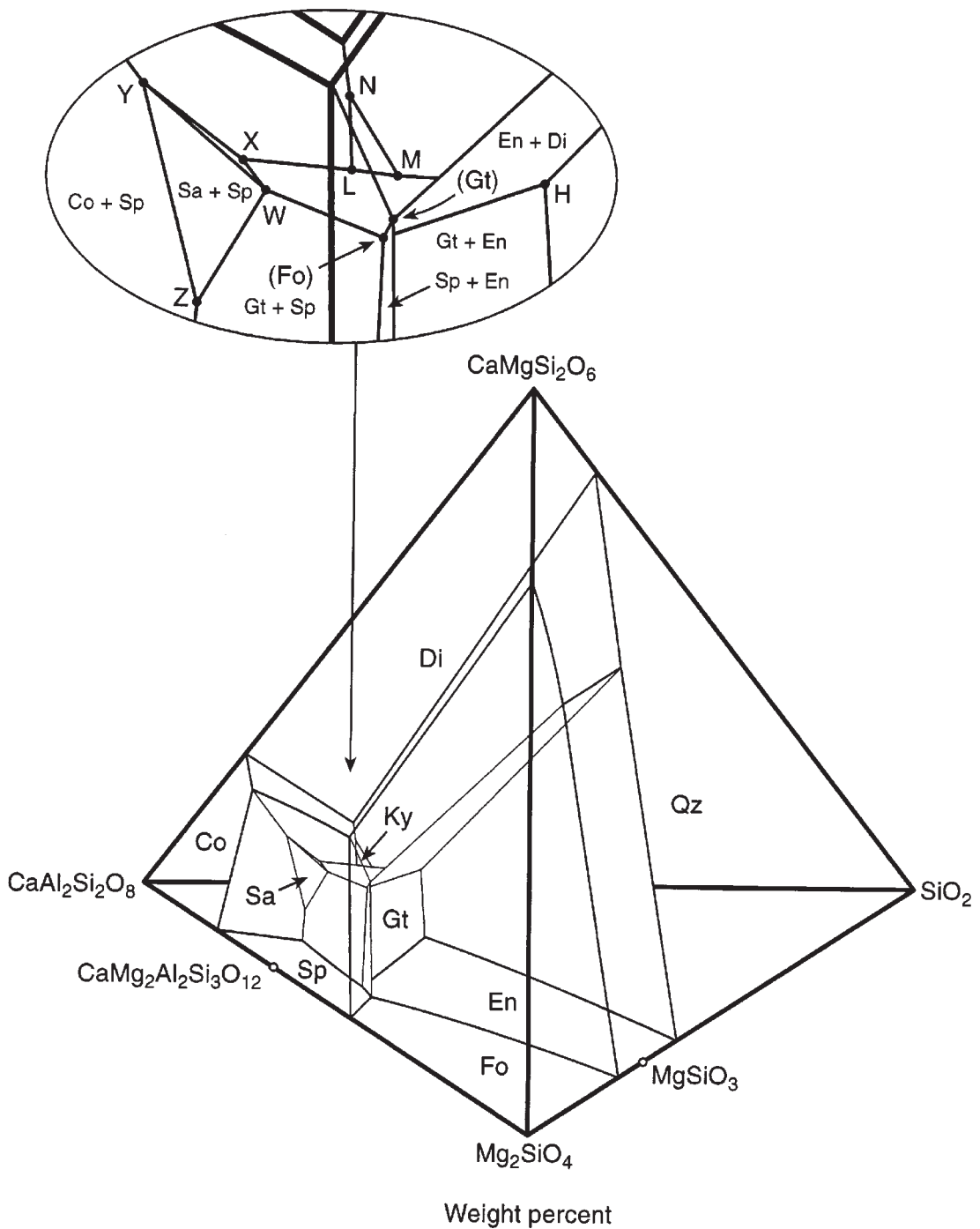


**Fig. 13.** Liquidus phase relations as in Fig. 9 but at a pressure slightly <3.0 GPa. Invariant point labels in parentheses are keyed to the reactions in Fig. 10 and Table 8. Changes in phase boundary positions from Fig. 9 are exaggerated for clarity. (See also Fig. 15a.)

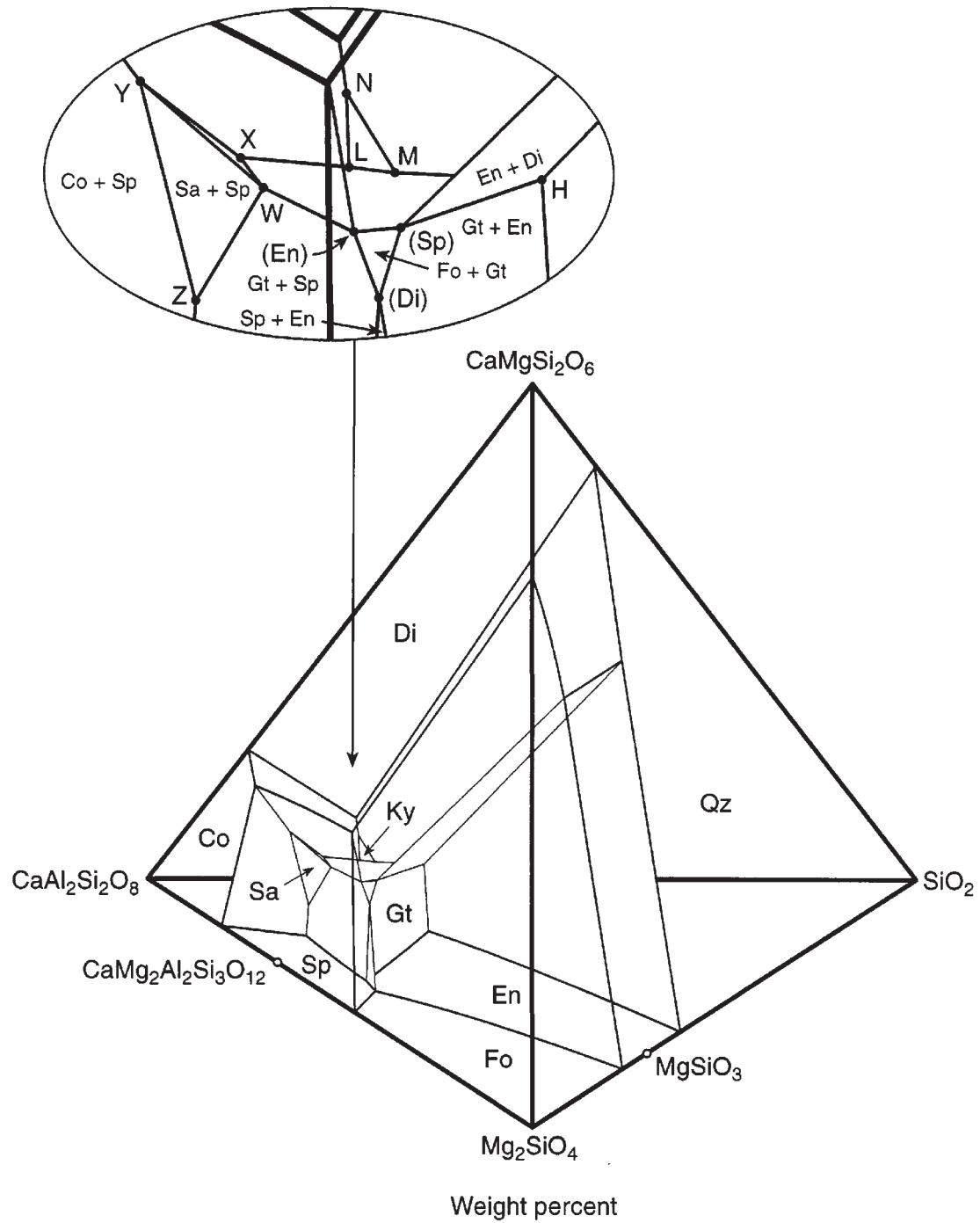


**Fig. 14.** Liquidus phase relations as in Fig. 9 but at a pressure slightly  $>3.0$  GPa. Invariant point labels in parentheses are keyed to the reactions in Fig. 10 and Table 8. Changes in phase boundary positions from Fig. 9 are exaggerated for clarity. (See also Fig. 15b.)

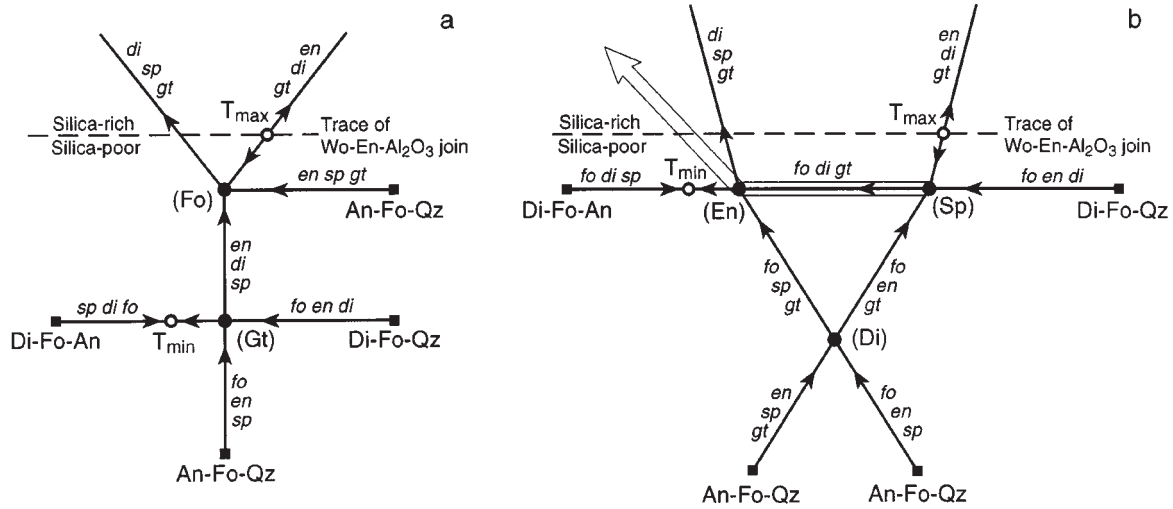


**Fig. 15.** Schairer diagrams showing schematic arrangement of liquidus invariant points (●) and univariant lines at a pressure slightly <math>< 3.0\text{ GPa}</math> (a) and slightly >math>> 3.0\text{ GPa}</math> (b). Invariant points labeled according to the absent crystalline phase in parentheses (see Table 8) and univariant lines labeled according to the crystalline phases present. Arrows indicate directions of decreasing temperature. Black squares label faces of the tetrahedron (Figs 13 and 14) intersected.

phase relations in the CMAS system are a very good guide to phase relations of natural lherzolite.

### ABSENCE OF ENSTATITE AT THE PERIDOTITE SOLIDUS

Takahashi (1986) and Walter (1998) have shown that enstatite disappears from the solidus of natural lherzolite at high pressures, beginning at  $\sim 3.3\text{ GPa}$ . Zhang & Herzberg (1994) also observed the absence of enstatite at the solidus at high pressures but did not determine the pressure at which this first occurs. Takahashi (1986) pointed out that the disappearance of enstatite is caused by the strong decrease of the CaO content of diopside at higher pressures and temperatures. The data of Walter (1998) show that even though enstatite is absent at the solidus and for a small temperature interval above the solidus at pressures  $> 3.3\text{ GPa}$ , it crystallizes as temperature is raised further and then dissolves at still higher temperatures. The melting behavior observed by Walter (1998) can be understood from the phase relations shown in Figs 14 and 15b. For melting at the solidus in the absence of enstatite, the initial melt occurs on the univariant line (En)–(Sp) in equilibrium with forsterite, diopside, and garnet. As temperature increases, the liquid moves up-temperature along the univariant line to the invariant point (Sp). At this point, enstatite is produced by melting of forsterite, diopside, and garnet (Table 8). As temperature increases above that of point (Sp), garnet is completely consumed and the liquid moves toward the Di–Fo–Qz face along the fo–en–di–liq boundary line (Figs 14 and 15b). During this stage of melting, diopside

and enstatite dissolve on heating and eventually leave only olivine in equilibrium with liquid. Thus, although enstatite is absent for a temperature interval at the beginning of melting, it is present for a significant temperature interval on further heating, exactly as observed by Walter (1998) for lherzolite KR4003. This consistency provides additional support for the argument made in the previous section that the CMAS system models the melting behavior of lherzolite very well.

### ALUMINOUS PYROXENE THERMAL DIVIDE

Yoder & Tilley (1962) suggested the existence of a high-pressure thermal divide that would lead to the production of tholeiitic magmas at low pressures and alkalic magmas at high pressures. Soon after this, O'Hara & Yoder (1963) were the first to identify the aluminous pyroxene plane (Figs 1, 2, 5, 9, 11, and 12) explicitly as a high-pressure thermal divide. They observed that as pressure increases, the forsterite primary phase volume shrinks to the  $\text{SiO}_2$ -poor side of the plane, thus causing melts generated from a garnet lherzolite to be trapped behind this plane and unable to penetrate it by fractional crystallization at these high pressures. Subsequent papers (O'Hara, 1965, 1968; O'Hara & Yoder, 1967; Kushiro & Yoder, 1974; Maaløe & Wyllie, 1979) provided further discussions and additional data to clarify the relevant phase relations. On the basis of data available at that time, Kushiro & Yoder (1974) placed invariant point P at  $\sim 2.5\text{ GPa}$  on the  $\text{SiO}_2$ -rich side of the aluminous pyroxene plane. They argued that on further shrinkage of the olivine volume with

pressure, the plane would become a thermal divide at a pressure between 2.6 and 3.0 GPa just as invariant point P moves across the plane to the SiO<sub>2</sub>-poor side. Additional discussion of the topology of these phase relations has been given by O'Hara (1969a, 1969b).

Our location of invariant point P at 3.0 GPa increases the pressure at which the thermal divide becomes effective. Details are illustrated in Figs 12, 14, and 15b. In Figs 14 and 15b at a pressure slightly above 3.0 GPa, a liquid generated at invariant point (Sp) from a model garnet lherzolite would move, on fractional crystallization, from (Sp) to (En) by crystallization of forsterite, diopside, and garnet. On further cooling from (En), the liquid would not move down a univariant line but would instead move directly across the diopside-spinel divariant surface in the direction shown by the arrow from point P in Fig. 12. This direction is the same as that indicated (at a pressure slightly >3.0 GPa) by the open arrow leaving point (En) in Fig. 15b. To determine this direction, we have used the phase compositions in equilibrium with liquid P (Table 6) in conjunction with the algebraic methods described by Presnall (1986). Thus, the thermal divide fails after the liquid path leaves (En) because spinel is one of the crystallizing phases.

In general, only those portions of the aluminous pyroxene plane that are ternary maintain the viability of the thermal divide. Stated another way, those portions that crystallize only phases that lie on the aluminous pyroxene plane (enstatite, diopside, garnet) enforce the thermal divide. Portions of the plane that are not ternary (i.e. crystallize a phase not lying on the plane) do not behave as a thermal divide. Spinel is the only phase in this category. Because spinel lies on the silica-poor side of the plane (Fig. 1), liquids on the non-ternary part of the plane will always crystallize spinel, with or without other phases, and move off the plane toward the silica-rich side. Liquids that show this behavior are defined by the boundaries of the spinel field in Figs 7 and 8.

An obvious question concerns the viability of the thermal divide at still higher pressures. Our data show that the garnet primary phase volume progressively expands with pressure relative to the primary phase volumes of enstatite, forsterite, and spinel. If this expansion continues, as expected, at higher pressures, the isobarically univariant line (Sp)-(En) (Figs 14 and 15b) will move closer to forsterite and the spinel volume will shrink. Thus, crystallization of spinel will be suppressed and the importance of crystallization of the forsterite-diopside-garnet assemblage will be enhanced. At a pressure just above 3.0 GPa, such crystallization is in the direction of strong SiO<sub>2</sub> depletion, but because this trend ends as soon as invariant point (En) is encountered, the effectiveness of the thermal divide depends on the contraction of the spinel primary phase volume. Thus, the influence of the thermal divide is expected to be

progressively strengthened as pressure increases above 3 GPa.

## FRACTIONATION OF KOMATIITIC AND PICRITIC MAGMAS

Komatiites have compositions that lie on the silica-poor side of the aluminous pyroxene thermal divide (Figs 2, 5, 9, 11, and 12) and are commonly believed to be generated at pressures >3 GPa (e.g. Herzberg, 1992; Gudfinnsson & Presnall, 1996). Extremely magnesian picrites believed by some to be parental to Hawaiian tholeiites (Wright, 1984; Albarede, 1992) also lie on the silica-poor side of the aluminous pyroxene plane. As these magmas rise to the Earth's surface, two kinds of processes can be visualized. If the rate of ascent is rapid relative to the rate of crystallization, expansion of the olivine field as pressure decreases continuously holds the magma composition within the olivine field, the thermal divide is thereby ignored, and a strong trend of olivine control is produced that extends across the thermal divide to silica-rich compositions. For example, let us imagine that a magma is generated at a pressure >3 GPa in equilibrium with olivine, enstatite, diopside, and garnet. The magma composition will lie on the silica-poor side of the thermal divide. If this magma is transported to a much lower pressure of, say, 2 GPa, and if the rate of transport is so rapid that there is no opportunity for crystallization, then the magma composition will lie deep within an expanded olivine primary phase field. Only olivine would subsequently crystallize and the liquid path would pass across the thermal divide along a line extending from the forsterite apex (Figs 9, 11, and 12). Strong olivine-controlled trends are displayed most prominently by Hawaiian tholeiites, and if the parental magmas for the tholeiites are highly magnesian, as advocated by Wright (1984) and Albarede (1992), Hawaiian tholeiitic volcanism is an example of polybaric fractional crystallization that crosses the thermal divide. However, others (e.g. Clague *et al.*, 1995; Rhodes, 1995), favor parental magmas for Hawaiian tholeiites that lie on the silica-rich side of the thermal divide. In this case, the most magnesian portion of the Hawaiian olivine-controlled trend, which lies on the silica-poor side of the thermal divide, would be due merely to lavas rich in olivine phenocrysts. Despite the uncertainty about Hawaiian tholeiites, the komatiites of Gorgona Island (Aitken & Echeverria, 1984) and the Reliance Formation (Nisbet *et al.*, 1987) appear to be clear examples of eruptive processes sufficiently rapid to produce olivine-controlled fractionation trends that cross the thermal divide (Gudfinnsson & Presnall, 1996, fig. 11).

At the other extreme, if the ascent of a picritic or komatiitic magma is arrested or if it rises very slowly and

cools at a pressure  $>3$  GPa, our data indicate that the thermal divide would enforce a strong fractionation trend toward silica-undersaturated liquids that is driven by crystallization of olivine, diopside, and garnet (Figs 14 and 15b). Our study does not include  $\text{Na}_2\text{O}$  and  $\text{K}_2\text{O}$ , but in the mantle, an alkalic as well as a silica-undersaturated trend toward an alkalic picrite is implied. Because the effectiveness of the thermal divide is expected to increase with pressure, the strength of the silica-undersaturated alkalic trend would depend on the pressure of crystallization and the rate of magma ascent. It is interesting that these alternative schemes of olivine control vs silica depletion are very similar to those suggested long ago by O'Hara (1965, 1968) and O'Hara & Yoder (1963, 1967) on the basis of far less complete experimental data. However, the silica-undersaturated residual liquid suggested by O'Hara & Yoder (1967) is a kimberlite, not an alkalic picrite. Although a kimberlitic residual liquid is possibly the result of very extreme fractional crystallization, our data support the formation only of an alkalic picrite.

The well-documented examples of olivine-controlled trends that cross the thermal divide, coupled with the apparent scarcity or absence in the geologic record of fractionation trends toward an alkalic picrite, suggest that magma ascent is usually rapid enough to neutralize the thermal barrier. However, magmas that ascend slowly enough to fractionally crystallize at high pressures would be more likely to crystallize completely before they reach the Earth's surface. Many blind conduits may exist at great depths that are filled with alkalic picrites or their fractionation products. This would mask evidence of the fractionation trend toward alkalic picrite. Possibly the only record of such a fractionation trend would be xenoliths brought to the surface by other eruptions.

## ACKNOWLEDGEMENTS

D. C. P. thanks Professor Ikuo Kushiro for provided financial support and an excellent working and living environment at the Institute for Study of the Earth's Interior, Okayama University, Misasa, Japan, during manuscript preparation. We thank D. Draper and the journal reviewers, M. J. O'Hara, R. W. Luth, and M. Hirschmann, for careful reviews that led to a number of improvements. This work was supported by National Science Foundation Grants EAR-8816044 and EAR-9219159, and Texas Advanced Research Program Grants 3927, 009741-007, 009741-044, and 009741-046. This paper is Department of Geosciences, University of Texas at Dallas, Contribution 855.

## REFERENCES

- Adam, J., (1988). Dry, hydrous, and  $\text{CO}_2$ -bearing liquidus phase relationships in the CMAS system at 28 kb, and their bearing on the origin of alkali basalts. *Journal of Geology* **96**, 709–719.
- Aitken, B. G. & Echeverria, L. M., (1984). Petrology and geochemistry of komatiites and tholeiites from Gorgona Island, Colombia. *Contributions to Mineralogy and Petrology* **86**, 94–105.
- Albarede, F., (1992). How deep do common basaltic magmas form and differentiate? *Journal of Geophysical Research* **97**, 10997–11009.
- Andersen, O., (1915). The system anorthite–forsterite–silica. *American Journal of Science* **39**, 407–454.
- Baker, M. B. & Stolper, E. M., (1994). Determining the composition of high-pressure mantle melts using diamond aggregates. *Geochimica et Cosmochimica Acta* **58**, 2811–2827.
- Boyd, F. R. & England, J. L., (1964). The system enstatite–pyrope. *Carnegie Institution of Washington, Yearbook* **63**, 157–161.
- Chen, C.-H. & Presnall, D. C., (1975). The system  $\text{Mg}_2\text{SiO}_4$ – $\text{SiO}_2$  at pressures up to 25 kilobars. *American Mineralogist* **60**, 398–406.
- Clague, D. A., Moore, J. G., Dixon, J. E. & Friesen, W. B., (1995). Petrology of submarine lavas from Kilauea's Puna Ridge, Hawaii. *Journal of Petrology* **36**, 299–349.
- Clark, S. P., Schairer, J. F. & de Neufville, J., (1962). Phase relations in the system  $\text{CaMgSi}_2\text{O}_6$ – $\text{CaAl}_2\text{SiO}_6$ – $\text{SiO}_2$  at low and high pressure. *Carnegie Institution of Washington, Yearbook* **61**, 59–68.
- Davis, B. T. C. & Boyd, F. R., (1966). The join  $\text{Mg}_2\text{Si}_2\text{O}_6$ – $\text{CaMgSi}_2\text{O}_6$  at 30 kilobars pressure and its application to pyroxenes from kimberlites. *Journal of Geophysical Research* **71**, 3567–3576.
- Davis, B. T. C. & England, J. L., (1964). The melting of forsterite up to 50 kilobars. *Journal of Geophysical Research* **69**, 1113–1116.
- Davis, B. T. C. & Schairer, J. F., (1965). Melting relations in the join diopside–forsterite–pyrope at 40 kilobars and at one atmosphere. *Carnegie Institution of Washington, Yearbook* **64**, 123–126.
- Gasparik, T., (1984). Two-pyroxene thermobarometry with new experimental data in the system  $\text{CaO}$ – $\text{MgO}$ – $\text{Al}_2\text{O}_3$ – $\text{SiO}_2$ . *Contributions to Mineralogy and Petrology* **87**, 87–97.
- Gudfinnsson, G., (1995). Melt generation in the system  $\text{CaO}$ – $\text{MgO}$ – $\text{Al}_2\text{O}_3$ – $\text{SiO}_2$  at 24 to 34 kbar and the system  $\text{CaO}$ – $\text{MgO}$ – $\text{Al}_2\text{O}_3$ – $\text{SiO}_2$ – $\text{FeO}$  at 7 to 28 kbar. Ph.D. Dissertation, The University of Texas at Dallas, 96 pp.
- Gudfinnsson, G. & Presnall, D. C., (1995). Melting relations of model lherzolite in the  $\text{CaO}$ – $\text{MgO}$ – $\text{Al}_2\text{O}_3$ – $\text{SiO}_2$ – $\text{FeO}$  system at 7 to 28 kbar. *EOS Transactions, American Geophysical Union* **76**, F696.
- Gudfinnsson, G. & Presnall, D. C., (1996). Melting relations of model lherzolite in the system  $\text{CaO}$ – $\text{MgO}$ – $\text{Al}_2\text{O}_3$ – $\text{SiO}_2$  at 2.4 to 3.4 GPa and the generation of komatiites. *Journal of Geophysical Research* **101**, 27701–27709.
- Herzberg, C., (1992). Depth and degree of melting of komatiites. *Journal of Geophysical Research* **97**, 4521–4540.
- Holdaway, M. J., (1971). Stability of andalusite and the aluminum silicate phase diagram. *American Journal of Science* **271**, 97–131.
- Irvine, T. N., (1975). Olivine–pyroxene–plagioclase relations in the system  $\text{Mg}_2\text{SiO}_4$ – $\text{CaAl}_2\text{Si}_2\text{O}_8$ – $\text{KAlSi}_3\text{O}_8$ – $\text{SiO}_2$  and their bearing on the differentiation of stratiform intrusions. *Carnegie Institution of Washington, Yearbook* **74**, 492–500.
- Jenkins, D. M. & Newton, R. C., (1979). Experimental determination of the spinel peridotite to garnet peridotite inversion at 900°C and 1,000°C in the system  $\text{CaO}$ – $\text{MgO}$ – $\text{Al}_2\text{O}_3$ – $\text{SiO}_2$ , and at 900°C with natural garnet and olivine. *Contributions to Mineralogy and Petrology* **68**, 407–419.
- Kinzler, R. J. & Grove, T. L., (1992). Primary magmas of mid-ocean ridge basalts 1. Experiments and methods. *Journal of Geophysical Research* **97**, 6885–6906.

- Kushiro, I., (1968). Compositions of magmas formed by partial zone melting in the earth's upper mantle. *Journal of Petrology* **7**, 337–362.
- Kushiro, I., (1969). The system forsterite–diopside–silica with and without water at high pressures. *American Journal of Science* **267A**, 269–294.
- Kushiro, I., (1972). Determination of liquidus relations in synthetic silicate systems with electron probe analysis: the system forsterite–diopside–silica at 1 atmosphere. *American Mineralogist* **57**, 1260–1271.
- Kushiro, I. & Yoder, H. S., Jr, (1974). Formation of eclogite from garnet lherzolite: liquidus relations in a portion of the system  $\text{MgSiO}_3$ – $\text{CaSiO}_3$ – $\text{Al}_2\text{O}_3$  at high pressures. *Carnegie Institution of Washington, Yearbook* **73**, 266–269.
- Lindsley, D. H., (1968). Melting relations of plagioclase at high pressure. In: Isachsen, Y. W. (ed.) *Origin of Anorthosite and Related Rocks. New York State Museum Science Service Memoir* **18**, 39–46.
- Liu, T.-C. & Presnall, D. C., (1990). Liquidus phase relationships on the join anorthite–forsterite–quartz at 20 kbar with applications to basalt petrogenesis and igneous sapphirine. *Contributions to Mineralogy and Petrology* **104**, 735–742.
- Longhi, J., (1987). Liquidus equilibria and solid solution in the system  $\text{CaAl}_2\text{Si}_2\text{O}_8$ – $\text{Mg}_2\text{SiO}_4$ – $\text{CaSiO}_3$ – $\text{SiO}_2$  at low pressure. *American Journal of Science* **287**, 265–331.
- Maaloe, S. & Wyllie, P. J., (1979). The join grossularite–pyrope at 30 kb and its petrological significance. *American Journal of Science* **279**, 288–301.
- Malinovsky, I. Y., Godovikov, A. A., Doroshev, A. M. & Ran, E. N., (1976). Silicate systems at high temperatures and pressures in connection with the petrology of the upper mantle and lower layers of the earth's crust. In: Godovikov, A. A. (ed.) *Fiziko-Khimicheskiye Usloviya Protsesov Mineraloobrazuyushchikh Teoreticheskii Eksperimentalnyi Dannymi*. Novosibirsk: Akademiya Nauk SSSR, Sibirskoye Otdeleniye, Instituta Geologii i Geofiziki, pp. 555–570.
- Nisbet, E. G., Arndt, N. T., Bickle, M. J., Cameron, W. E., Chauvel, C., Cheadle, M., Hegner, E., Kyser, T. K., Martin, A., Renner, R. & Roedder, E., (1987). Uniquely fresh 2.7 Ga komatiites from the Belingwe greenstone belt, Zimbabwe. *Geology* **15**, 1147–1150.
- O'Hara, M. J., (1963). The join diopside–pyrope at 30 kilobars. *Carnegie Institution of Washington, Yearbook* **62**, 116–118.
- O'Hara, M. J., (1965). Primary magmas and the origin of basalts. *Scottish Journal of Geology* **1**, 19–40.
- O'Hara, M. J., (1968). The bearing of phase equilibria studies in synthetic and natural systems on the origin and evolution of basic and ultrabasic rocks. *Earth-Science Reviews* **4**, 69–133.
- O'Hara, M. J., (1969a). The relationship between liquid and crystals in univariant equilibria of four component systems, their application to the origin and melting of ultramafic rocks and refractories. In: *Progress in Experimental Petrology, First Report, NERC Supported Research Units in British Universities, 1965–1968*, pp. 114–120.
- O'Hara, M. J., (1969b). Quaternary invariant equilibria involving liquid; their application to the origin of mafic and ultramafic nodules in igneous rocks. In: *Progress in Experimental Petrology, First Report, NERC Supported Research Units in British Universities, 1965–1968*, pp. 120–128.
- O'Hara, M. J. & Yoder, H. S., Jr, (1963). Partial melting of the mantle. *Carnegie Institution of Washington, Yearbook* **62**, 66–71.
- O'Hara, M. J. & Yoder, H. S., Jr, (1967). Formation and fractionation of basic magmas at high pressures. *Scottish Journal of Geology* **3**, 67–117.
- O'Hara, M. J., Richardson, S. W. & Wilson, G., (1971). Garnet–peridotite stability and occurrence in crust and mantle. *Contributions to Mineralogy and Petrology* **32**, 48–68.
- Presnall, D. C., (1976). Alumina content of enstatite as a geobarometer for plagioclase and spinel lherzolites. *American Mineralogist* **61**, 582–588.
- Presnall, D. C., (1986). An algebraic method for determining equilibrium crystallization and fusion paths in multicomponent systems. *American Mineralogist* **71**, 1061–1070.
- Presnall, D. C., (1991). Algebraic methods for determining directions of decreasing temperature along isobaric liquidus univariant lines. *Canadian Mineralogist* **92**, 687–692.
- Presnall, D. C., Simmons, C. L. & Porath, H., (1972). Changes in electrical conductivity of a synthetic basalt during melting. *Journal of Geophysical Research* **77**, 5665–5672.
- Presnall, D. C., Dixon, S. A., Dixon, J. R., O'Donnell, T. H., Brenner, N. L., Schrock, R. L. & Dycus, D. W., (1978). Liquidus phase relations on the join diopside–forsterite–anorthite from 1 atm to 20 kbar; their bearing on the generation and crystallization of basaltic magma. *Contributions to Mineralogy and Petrology* **66**, 203–220.
- Presnall, D. C., Dixon, J. R., O'Donnell, T. H. & Dixon, S. A., (1979). Generation of mid-ocean ridge tholeiites. *Journal of Petrology* **20**, 3–35.
- Presnall, D. C., Weng, Y.-H., Milholland, E. C. S. & Walter, M. J., (1998). Liquidus phase relations in the system  $\text{MgO}$ – $\text{MgSiO}_3$  at pressures up to 25 GPa—constraints on crystallization of a molten Hadean mantle. *Physics of the Earth and Planetary Interiors*. In press.
- Preston-Thomas, H., (1990). The International Temperature Scale of (1990) (ITS-90). *Metrologia* **27**(3–10), 107.
- Rhodes, J. M., (1995). The 1852 and 1868 Mauna Loa picrite eruptions: clues to parental magma compositions and the magmatic plumbing system. In: Rhodes, J. M. & Lockwood, J. P. (eds) *Mauna Loa Revealed: Structure, Composition, History, and Hazards. Geophysical Monograph, American Geophysical Union* **92**, 241–262.
- Sen, G. & Presnall, D. C., (1984). Liquidus phase relationships on the join anorthite–forsterite–quartz at 10 kbar with applications to basalt petrogenesis. *Contributions to Mineralogy and Petrology* **85**, 404–408.
- Stolper, E., (1980). A phase diagram for mid-ocean ridge basalts: preliminary results and implications for petrogenesis. *Contributions to Mineralogy and Petrology* **74**, 13–27.
- Takahashi, E., (1986). Melting of a dry peridotite KLB-1 up to 14 GPa: implications on the origin of peridotitic upper mantle. *Journal of Geophysical Research* **91**, 9367–9382.
- Walter, M. J., (1998). Melting of garnet peridotite and the origin of komatiite and depleted lithosphere. *Journal of Petrology* **39**, 29–60.
- Walter, M. J. & Presnall, D. C., (1994). Melting behavior of simplified lherzolite in the system  $\text{CaO}$ – $\text{MgO}$ – $\text{Al}_2\text{O}_3$ – $\text{SiO}_2$ – $\text{Na}_2\text{O}$  from 7 to 35 kbar. *Journal of Petrology* **35**, 329–359.
- Walter, M. J., Sisson, T. W. & Presnall, D. C., (1995). A mass proportion method for calculating melting reactions and application to melting of model upper mantle lherzolite. *Earth and Planetary Science Letters* **135**, 77–90.
- Weng, Y.-H. & Presnall, D. C., (1995). Constraints on the depth of origin of komatiites based on melting relations in the system  $\text{CaO}$ – $\text{MgO}$ – $\text{Al}_2\text{O}_3$ – $\text{SiO}_2$  at 5 GPa. *EOS Transactions, American Geophysical Union* **76**, F696–F697.
- Wright, T. L., (1984). Origin of Hawaiian tholeiite: a metasomatic model. *Journal of Geophysical Research* **89**, 3233–3252.
- Yoder, H. S., Jr & Tilley, C. E., (1962). Origin of basalt magmas: an experimental study of natural and synthetic rock systems. *Journal of Petrology* **3**, 342–532.
- Zhang, J. & Herzberg, C., (1994). Melting experiments on anhydrous peridotite KLB-1 from 5.0 to 22.5 GPa. *Journal of Geophysical Research* **99**, 17729–17742.